Original paper

(Fe,Mn)–(Ti,Sn)–(Nb,Ta) oxide assemblage in a little fractionated portion of a mixed (NYF + LCT) pegmatite from Piława Górna, the Sowie Mts. block, SW Poland

Adam PIECZKA[1*], Adam SZUSZKIEWICZ[2], Eligiusz SZEŁĘG[3], Krzysztof NEJBERT[4],
Marek ŁODZIŃSKI[5], Sławomir ILNICKI[4], Krzysztof TURNIAK[2], Magdalena BANACH[6],
Władysław HOŁUB[6], Piotr MICHAŁOWSKI[6], Roman RÓŻNIAK[6]

[1] AGH University of Science and Technology, Department of Mineralogy, Petrography and Geochemistry 30-059 Kraków, Mickiewicza 30, Poland; pieczka@agh.edu.pl

[2] University of Wrocław, Institute of Geological Sciences, 50-205 Wrocław, Cybulskiego 30, Poland

[3] University of Silesia, Faculty of Earth Sciences, Department of Geochemistry, Mineralogy and Petrography, 41-200 Sosnowiec, Będzińska 60, Poland

[4] University of Warsaw, Faculty of Geology, Institute of Geochemistry, Mineralogy and Petrology, 02-089 Warszawa, Żwirki and Wigury 93, Poland

[5] AGH University of Science and Technology, Department of General Geology and Geotourism, 30-059 Kraków, Mickiewicza 30, Poland

[6] DSS Company, Piława Górna Quarry, 58-240 Piława Górna, Sienkiewicza 96, Poland

* Corresponding author

Textural relationships and compositional variations of (Fe,Mn)–(Ti,Sn)–(Nb,Ta) oxides and associated minerals from low- to moderately fractionated, mixed (NYF + LCT) anatectic pegmatites, which belong to the Julianna pegmatitic system, exposed at Piława Górna, Lower Silesia, Poland, were studied to elucidate the geochemical evolution of the pegmatite-forming melt. The primary Nb–Ta oxides crystallized in the following sequence: (1) columbite-(Fe) evolving to columbite-(Mn), associated with Nb- and Ta-bearing ilmenite–pyrophanite + almandine–spessartine garnet + Ti-poor schorl, (2) columbite-(Fe), (3) tantalite-(Fe), (4) Ti- and Sn-bearing ixiolite ± ferrowodginite ± Nb- and Ta-bearing cassiterite ± columbite-(Fe), all crystallizing along with Ti-enriched schorl evolving to dravite. The most characteristic features of the mineral assemblages are the reversed Mn–Fe fractionation trends and increasing Ca concentrations at the final stage of crystallization. These compositional variations are explained by a possible pre-emplacement contamination of the pegmatite-forming melt and re-equilibration of biotite and plagioclase from the early-crystallized outer zones of the pegmatites with rapidly cooling pegmatitic melt. Local changes in melt composition were of minor importance. Late alterations, such as chloritization and muscovitization of biotite or albitization of Ca-rich plagioclase were significant only at the hydrothermal stage.

Keywords: Nb–Ta oxides, mixed NYF + LCT anatectic pegmatites, compositional evolution, reversed Mn–Fe fractionation, Piława Górna, Poland
Received: 20 February 2013; accepted: 29 May 2013; handling editor: R. Škoda

1. Introduction

Pegmatites of the Góry Sowie Mountains block (GSB) in Lower Silesia, Poland, have been known for over 200 years. In the 1700s and 1800s, numerous pegmatitic bodies were mined as a source of raw quartz and feldspar. Historical literature noted the presence of several mineral phases, such as perfectly developed, large crystals of black tourmaline, light-greenish beryl, microcline, rare phosphate minerals as triplite, huréaulite and vivianite, and columbite (Fiedler 1863; Römer 1864; Roth 1867; Traube 1888; Dathe and Finckh 1924; Hintze 1933). The pegmatite at Michałkowa (= *Michelsdorf*) is the type locality for sarcopside (Websky 1868). The end of mining activity in the area has limited modern mineralogical

studies to a few small *in situ* occurrences, old mining dumps and museum specimens. Nonetheless, a number of minerals have been described, including Li-bearing phosphates, elbaite, and columbite-(Fe) and Pb-bearing microlite occurring as inclusions in beryl (Pieczka et al. 2003, 2004; Łodziński and Pieczka 2008). Novák (2005), in his paper summarizing the current state of knowledge of the Bohemian Massif pegmatites, classified the GSB pegmatites as the beryl subtype of the LCT (*lithium–cesium–tantalum*) petrogenetic family of Černý and Ercit (2005).

In the 2007, the Dolnośląskie Surowce Skalne S.A Company, one of the largest Polish suppliers of crushed rock aggregates, opened a new quarry near the town of Piława Górna and uncovered the largest pegmatitic

system known in the GSB. The system, named Julianna, displays a hybrid geochemical signature (Pieczka et al. 2012; Szuszkiewicz et al. in print). Commonly low- to moderately evolved pegmatites contain minerals typical of the NYF (*niobium–yttrium–fluorine*) petrogenetic family. However, the pegmatites only exceptionally attain a very high degree of geochemical evolution, and also contain typical LCT-signature minerals. Recently, Novák et al. (2012) described pegmatites from Bližná and Kracovice, Czech Republic, as representatives of such a mixed NYF + LCT signature in the Moldanubian Zone.

This paper describes in detail the textural relationships and compositional evolution of the primary (Fe,Mn)–(Ti,Sn)–(Nb,Ta) assemblage and associated minerals in the low- to moderately evolved pegmatites that largely dominate the Julianna system at Piława Górna (Szełęg et al. 2010; Szuszkiewicz et al. in print). The results are discussed as potential indicators of processes controlling the geochemical evolution of the pegmatite-forming melt. The corresponding mineral assemblage from exceptionally rare, highly-evolved, Li–Cs–Ta–Be–B mineralized portions of some of the largest pegmatitic veins will be the subject of a separate study.

2. Geological setting

The GSB occupies the central portion of the Sudetes, SW Poland, in the northeastern part of the Bohemian Massif (Fig. 1). The unit is built predominantly by oligoclase–biotite paragneisses, migmatites and orthogneisses, with minor intercalations of anatectic granites and pegmatites, metabasites, granulites, eclogites, marbles and calc-silicate rocks (Polański 1955; Grocholski 1967; Morawski 1973; Kryza 1981; Żelaźniewicz 1987; Gunia 1997; Ilnicki et al. 2010). A greywacke pelitic–psammitic sequence of late Proterozoic to early Cambrian age (Gunia 1985) and I-type, calc-alkaline igneous rocks dated at 518–480 Ma (Kröner and Hegner 1998; Kryza and Fanning 2007) are considered protoliths to the gneisses.

The GSB gneissic complex underwent a polymetamorphic evolution. An older HP–HT metamorphism at ~400 Ma (Brueckner et al. 1996; O'Brien et al. 1997; Kryza and Fanning 2007) was followed by high amphibolite-facies overpint (Kryza 1981; Żelaźniewicz 1987, 1990, 1997). Five tectonothermal events (D_1–D_5) have been recognized in the gneissic–amphibolite suite and the peak metamorphic conditions were ascribed to stages D_2–D_3 (Żelaźniewicz 1990). The subsequent decompression caused local partial melting at ~380–370 Ma, leading to the formation of anatectic pegmatites, granites, aplites and quartz veins (van Breemen et al. 1988; Bröcker et

al. 1998; Timmermann et al. 2000; Aftalion and Bowes 2002; Gordon et al. 2005).

The town of Piława Górna is located ~50 km southwest of Wrocław in the eastern part of the GSB. This fragment of the GSB belongs to the Fore-Sudetic Block, the strongly peneplained NE margin of the Sudetes (Fig. 1). A quarry about 100 m deep, owned by the Dolnośląskie Surowce Skalne S.A Company, is situated 1.5 km to the north-west of the town (50°42′11.77″N; 16°44′12.36″E) and exploits a large migmatite–amphibolite deposit (~ 380 million metric tons) for crushed rock aggregates. Migmatitic gneisses composed of quartz, K-feldspars, biotite, subordinate muscovite, garnet, and accessory zircon, apatite and sillimanite, are commonly cut discordantly by leucosome segregations, which in places may be treated as *syn*-migmatitic pegmatitic granite. Weakly foliated amphibolites, identified as retrogressed eclogite, are built by hornblende and plagioclase with minor garnet, locally abundant biotite, subordinate ilmenite, rutile, clinozoisite, quartz, and accessory relics of clinopyroxene and spinel (Ilnicki et al. 2010). The rocks are cut discordantly by a number of anatectic pegmatite dikes, which intruded tectonized amphibolite. The largest pegmatitic bodies, up to 6 m thick, were exposed along 30–40 m in the vertical, and 80–100 m in the longitudinal sections (fig. 4 in Szuszkiewicz et al. in print). They typically display a low to moderate degree of geochemical fractionation with enhanced Nb–REE–Be–B contents and consist mainly of microcline, plagioclase (oligoclase–andesine and albite), quartz, biotite and muscovite accompanied by common schorl, garnet and beryl. An idealized zone sequence begins with a discontinuous, fine- to medium-grained granitic *border zone* up to a few centimeters thick that is succeeded by a coarser grained *wall zone* with distinct unidirectional growth textures, a *graphic intermediate zone* composed of feldspar–quartz intergrowths and characteristic giant biotite laths (up to 60 cm long), and a *blocky feldspar intermediate zone* formed mainly of microcline with subordinate oligoclase–albite. The total thickness of the border and wall zones reaches ~ 0.3 m, whilst both intermediate zones attain a thickness of *c.* 2 m. Several decimeter- to meter-sized *quartz cores* occur as pockets or lenses roughly along the axial portions of larger dykes. Various Nb–Ta minerals, including columbite-group minerals, ixiolite, ferrowodginite, samarskite-, euxenite- and fergusonite-group minerals, pyrochlore-supergroup minerals, and also Nb- and Ta-enriched varieties of cassiterite, ilmenite and titanite, constitute important accessory minerals and many of them suggest a NYF signature for the parental melt. However, in exceptionally rare cases, when fractionation attained a very high degree, the LCT-signature mineral assemblage including elbaite–liddicoatite, pollucite, spodumene, Cs-beryl and Li-micas is encountered
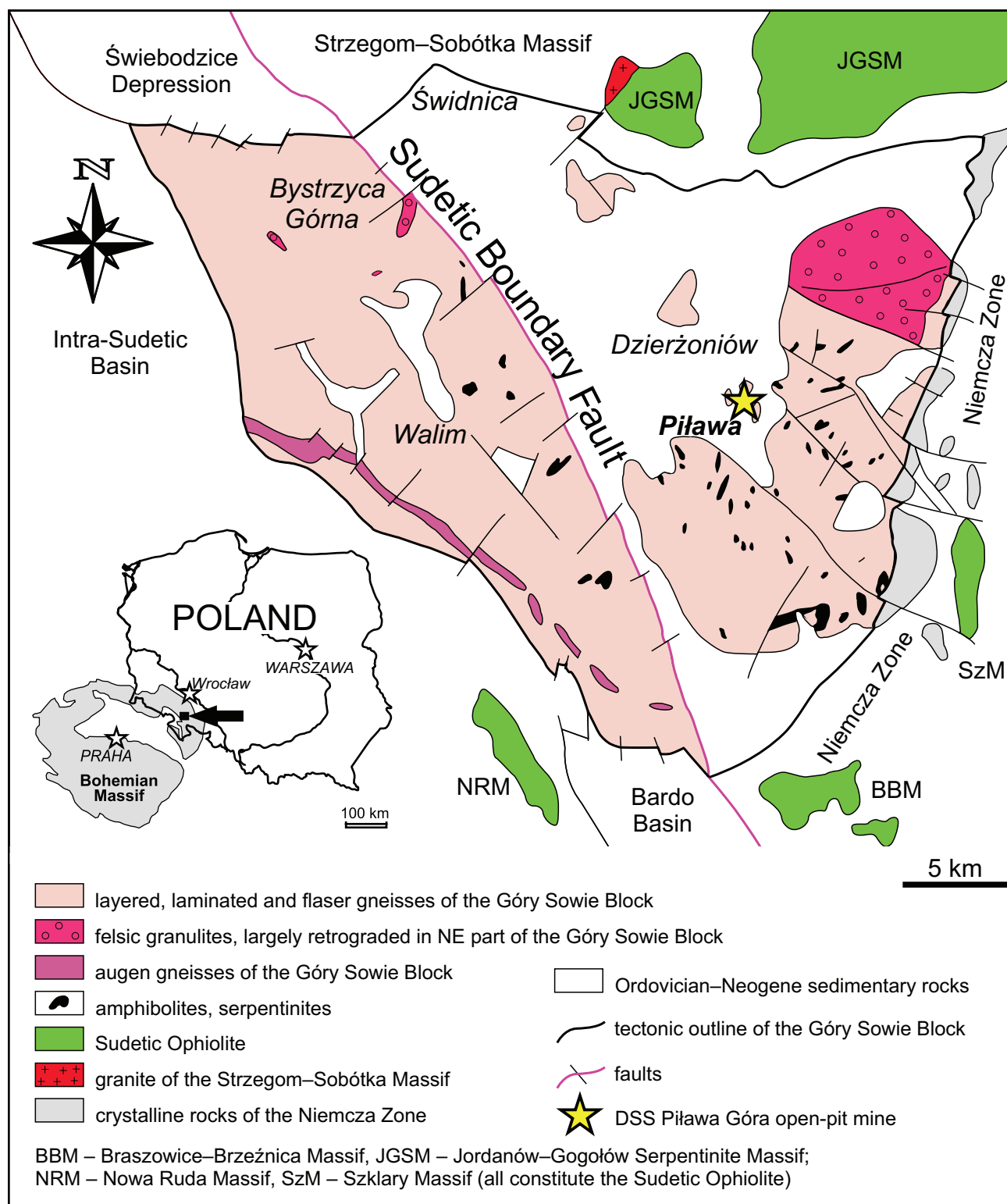
Fig. 1 Geological map of the Góry Sowie Block (after Szuszkiewicz et al. in print).

(Łodziński et al. 2010; Nejbert et al. 2010; Pieczka et al. 2010, 2012; Szełęg et al. 2010). Thus the complex Julianna system of cogenetic pegmatites is tentatively assigned to the mixed NYF + LCT family (Pieczka et al. 2012; Szuszkiewicz et al. in print) of Černý and Ercit (2005).

3. Methods

3.1. Sampling

In the Piława Górna quarry, amphibolite and migmatite are quarried together with associated pegmatites by blasting to an amount of about 5 million metric tons per year. Such a large-scale exploitation results in very short average duration of an exposed pegmatitic body, usually a few days. Therefore, direct *in situ* observations of pegmatites were strongly limited and hand samples were mostly collected from loose blocks detached from the quarry wall after blasting. Although it was always possible to reconstruct the position of a sample within the overall zoning scheme of the pegmatite, identifying a very precise location for each of the analyzed crystals, for instance with reference to the distance from the pegmatite's margins, was not feasible.

3.2. Analytical procedures

Samples were prepared in the form of 1-inch discs containing the chosen crystals or crystal aggregates together with adjacent minerals, polished and carbon-coated. Electron microprobe analyses (EMPA) were performed at the Inter-Institute Analytical Complex for Minerals and Synthetic Substances of University of Warsaw with a CAMECA SX 100 electron microprobe in wavelength-dispersive (WDS) mode. Operating conditions were: accelerating voltage of 20 kV, beam current of 20 nA, beam diameter of 2 μm, peak count time of 20 s and background time of 10 s. The following standards, analytical lines and crystals were used: apatite – F (K_α, TAP), albite – Na (K_α, TAP), diopside – Mg (K_α, TAP) and Si (K_α, TAP), orthoclase – Al (K_α, TAP) and K (K_α, LIF), wollastonite – Ca (K_α, PET), Sc pure – Sc (K_α, PET), rutile – Ti (K_α, PET), V_2O_5 – V (K_α, LIF), rhodonite – Mn (K_α, LIF), hematite – Fe (K_α, LIF), sphalerite – Zn (K_α, LIF), YAG – Y (L_α, PET), zircon – Zr (L_α, PET), Nb pure – Nb (L_α, PET), cassiterite – Sn (L_α, PET), barite – Ba (L_α, PET), LaP_5O_{14} – La (L_α, PET), CeP_5O_{14} – Ce (L_α, PET), Ta pure – Ta (M_α, TAP), W pure – W (M_β, TAP), galena – Pb (M_α, PET), Bi_2Te_3 – Bi (M_α, PET), U_3O_8 – U (M_α, TAP), ThO_2 – Th (M_α, PET). The raw data were reduced with the PAP routine (Pouchou and Pichoir 1985). For comparison of atomic abundances in the studied oxides, the formulae of columbite-group minerals (CGM), ixiolite, ferrowodginite and cassiterite have been normalized to 24 oxygen atoms per formula unit (*apfu*), assuming valence charge-balance and a value of the Fe^{3+}/Fe_{total} ratio such as to reduce any surplus in the cation totals over 12 *apfu*, i.e., above the number of the structurally available lattice positions. Thus, the formula of ferrowodginite was taken as $A_3B_3C_6O_{24}$, instead of

$A_4B_4C_8O_{32}$, ixiolite as $(A,B,C)_{12}O_{24}$, and CGM as $A_4D_8O_{24}$, where *A* denotes Fe^{2+}, Mn, Ca, Mg, and additionally Li^+ with vacancies in the wodginite-group minerals (WGM), *B* – Sn, Ti, Zr, Hf, Fe^{3+}, Sc and additionally Ta excess in WGM, *C* – Nb, Ta and W, whilst *D* includes simultaneously both the *B* and *C* components. For distinguishing between minerals of the columbite group, ixiolite and ferrowodginite, only the stoichiometric criteria suggested by Wise et al. (1998) were employed. Accordingly, the term *ixiolite* was used only for samples with more than 10 mol. % SnO_2 + TiO_2 + ZrO_2 + HfO_2 + Sc_2O_3 + Fe_2O_3, i.e. > 1.2 (R^{3+} + R^{4+}) *pfu*, and which do not match the criteria for completely ordered WGM, i.e. Ta ≥ 2 Nb at the *C* site, the sum of *B*-site cations Sn + Ti + Zr + Hf + Sc + Fe^{3+} ≤ 0.5 Ta + Nb + W, and Ti + Sn + Zr + Hf + Sc + Fe^{3+} + Ta_{excess} in *C* = 3 *apfu* according to Ercit et al. (1992).

The compositions of pyrochlore-supergroup minerals were normalized to 2 *B* = (Nb + Ta + Ti + W + Sn + Zr + Al + Fe^{3+}) *apfu*, with traces of Si treated as an impurity located outside the pyrochlore structure. All Fe was treated as Fe^{3+}. The H_2O was calculated by stoichiometry in two alternative ways: (1) for the case of OH existing in the *X* site, i.e. when the O equivalent ($O_{eq.}$) equals to half of the total cation charge < 6, and (2) when OH exists in the *Y* site, i.e. for 6.5 ≥ $O_{eq.}$ > 6, with an assumption that O^{2-} can appear in the *Y* site only when 7 ≥ $O_{eq.}$ > 6.5.

The composition of ilmenite has been normalized to 3 O *pfu*, and the compositions of the coexisting tourmaline supergroup and garnet group minerals to 31 (O,OH,F) and 15 (*Y* + *Z* + *T*) cations, and 12 O, respectively. Biotite compositions were normalized to 22 O *pfu*. All Fe was treated as Fe^{2+} and OH^- was calculated by stoichiometry.

The entire set of the EMP data includes *c.* 600 spot analyses of CGM and ixiolite, 25–30 analyses of ferrowodginite, cassiterite, ilmenite and minerals of the pyrochlore supergroup each, and 60 analyses for each of tourmaline and garnet, and *c.* 80 analyses of biotite.

4. Mineralogy of the Nb–Ta assemblage

In the little fractionated portion of the Julianna pegmatitic system, (Fe,Mn)–(Ti,Sn)–(Nb,Ta) oxides are represented by columbite-group minerals, titanian and stannian ixiolite, ferrowodginite, members of the pyrochlore supergroup, Nb–Ta-bearing varieties of the ilmenite-group minerals and cassiterite.

4.1. Columbite-group minerals

Minerals of the columbite group are the most widespread Nb–Ta phases, occurring from the inner graphic zone

Tab. 1a Representative compositions of a columbite crystal of fractionation style IIa

P116a	1	2	3	4	5	6	7	8	9	10
					wt. %					
WO_3	0.35	0.53	0.27	0.20	0.30	0.96	1.64	1.20	0.70	0.73
Nb_2O_5	62.69	61.00	28.44	27.51	27.30	26.07	24.94	29.57	31.66	32.60
Ta_2O_5	16.27	18.78	52.49	53.32	53.10	51.60	49.10	46.79	45.07	44.83
TiO_2	0.68	0.66	1.00	0.92	0.89	1.09	1.50	1.75	2.42	2.61
ZrO_2	0.00	0.00	0.00	0.00	0.00	0.21	0.36	0.25	0.22	0.17
SnO_2	0.21	0.22	0.34	0.15	1.04	3.09	5.73	3.14	2.20	1.56
Sc_2O_3	0.03	0.04	0.12	0.13	0.11	0.10	0.15	0.15	0.20	0.20
Fe_2O_3	0.00	0.00	0.77	1.84	0.75	1.41	1.76	1.52	1.34	1.54
FeO	10.82	12.80	11.05	11.21	12.05	11.90	12.22	12.70	12.76	12.63
MnO	8.75	6.39	4.75	3.93	3.54	3.04	2.04	2.40	2.53	2.79
MgO	0.00	0.00	0.02	0.04	0.04	0.04	0.05	0.05	0.04	0.04
Total	99.80	100.42	99.26	99.26	99.12	99.51	99.46	99.52	99.14	99.68
				Content of ions on the basis of 24 O and 12 cations pfu						
Fe^{2+}	2.174	2.584	2.635	2.678	2.898	2.846	2.912	2.957	2.937	2.873
Mn^{2+}	1.781	1.306	1.147	0.951	0.862	0.736	0.492	0.567	0.590	0.643
Mg^{2+}	0.000	0.000	0.009	0.019	0.017	0.019	0.020	0.019	0.015	0.018
Sc^{3+}	0.006	0.008	0.031	0.033	0.027	0.024	0.037	0.037	0.048	0.047
ΣA site	*3.961*	*3.898*	*3.822*	*3.681*	*3.805*	*3.624*	*3.460*	*3.580*	*3.590*	*3.581*
W^{6+}	0.022	0.033	0.020	0.015	0.022	0.071	0.121	0.087	0.050	0.051
Nb^{5+}	6.810	6.655	3.667	3.552	3.548	3.371	3.213	3.723	3.939	4.010
Ta^{5+}	1.063	1.233	4.071	4.141	4.151	4.014	3.806	3.543	3.372	3.218
Ti^{4+}	0.124	0.120	0.216	0.198	0.191	0.234	0.322	0.366	0.501	0.534
Zr^{4+}	0.000	0.000	0.000	0.000	0.000	0.029	0.049	0.034	0.029	0.022
Sn^{4+}	0.020	0.022	0.038	0.017	0.119	0.352	0.651	0.349	0.242	0.169
Fe^{3+}	0.000	0.000	0.166	0.395	0.163	0.303	0.377	0.318	0.277	0.315
ΣB site	*8.039*	*8.061*	*8.178*	*8.319*	*8.195*	*8.376*	*8.540*	*8.420*	*8.410*	*8.419*
O^{2-}	24	24	24	24	24	24	24	24	24	24
Mn/(Mn+Fe)	*0.450*	*0.336*	*0.291*	*0.236*	*0.220*	*0.189*	*0.130*	*0.147*	*0.155*	*0.168*
Ta/(Ta+Nb)	*0.135*	*0.156*	*0.526*	*0.538*	*0.539*	*0.543*	*0.542*	*0.488*	*0.461*	*0.453*

through the blocky feldspar zone up to the quartz core, commonly in association with beryl, tourmaline and garnet, sometimes also with small crystals of zircon, titanite, cheralite, thorite and even with samarskite-group minerals and fergusonite-(Y). They form single, steel blue to black euhedral crystals ranging from needle-like forms to plates up to 7 cm long and 1 cm wide. The crystals are often randomly intergrown, and sometimes form rosettes (to 3–4 cm across) or string-like intergrowths up to 10 cm long. Many crystals of columbite-(Fe) show simple compositional growth-zoning visible in back-scattered-electron (BSE) images as a distinct dark-grey core overgrown by a lighter mantle (Figs 2a–b). Both the core and the mantle show second order oscillatory zoning resulting from subtle variations in Mn and Fe contents. This style of zoning is typical mainly of crystals showing undisturbed progressive Mn–Fe and Ta–Nb core-to-rim fractionation. Similar zoning in crystals obtained from the external portion of the blocky feldspar zone and associated with zircon, monazite, thorite and fergusonite-(Y) reflects the reversed Mn–Fe fractionation coupled with a very limited, progressive Ta–Nb fractionation. A more complex zoning pattern involving a few concentric bands with blurred boundaries, is less common (right part of a

crystal in Fig. 2c). Crystals with such an internal texture can be overgrown by, or partly replaced with, younger CGM evolving to tantalite-(Fe) with a higher Ta/(Nb + Ta) value (the lightest regions of crystals in Figs 2b–e). The latter seldom displays compositional variations in the final growth stage (Fig. 2f, inserts f1 and f2). None of the columbite crystals seen was intergrown with ilmenite-group minerals and intergrowths with cassiterite were only occasionally found.

Three different Mn–Fe vs. Ta–Nb fractionation paths reflected in single crystal core-to-rim zoning were distinguished on the basis of columbite crystals collected from different places in the blocky feldspar zone of a few veins with similar mineralogical and geochemical signatures (Fig. 3). They indicate that CGM evolution began with the crystallization of columbite-(Fe) at Mn/(Mn + Fe) close to 0.34–0.36 and Ta/(Ta + Nb) to 0.05–0.07 along a normal fractionation path towards columbite-(Mn) (trend I in Figs 3a–b). The highest Mn/(Mn + Fe) values slightly exceed 0.50. The Mn–Fe fractionation becomes subsequently reversed down to a Mn/(Mn + Fe) value a little below 0.20. The reversal takes place over a broad range of Ta/(Ta + Nb) values from 0.09 to 0.27, which probably reflects the various positions of the crystals
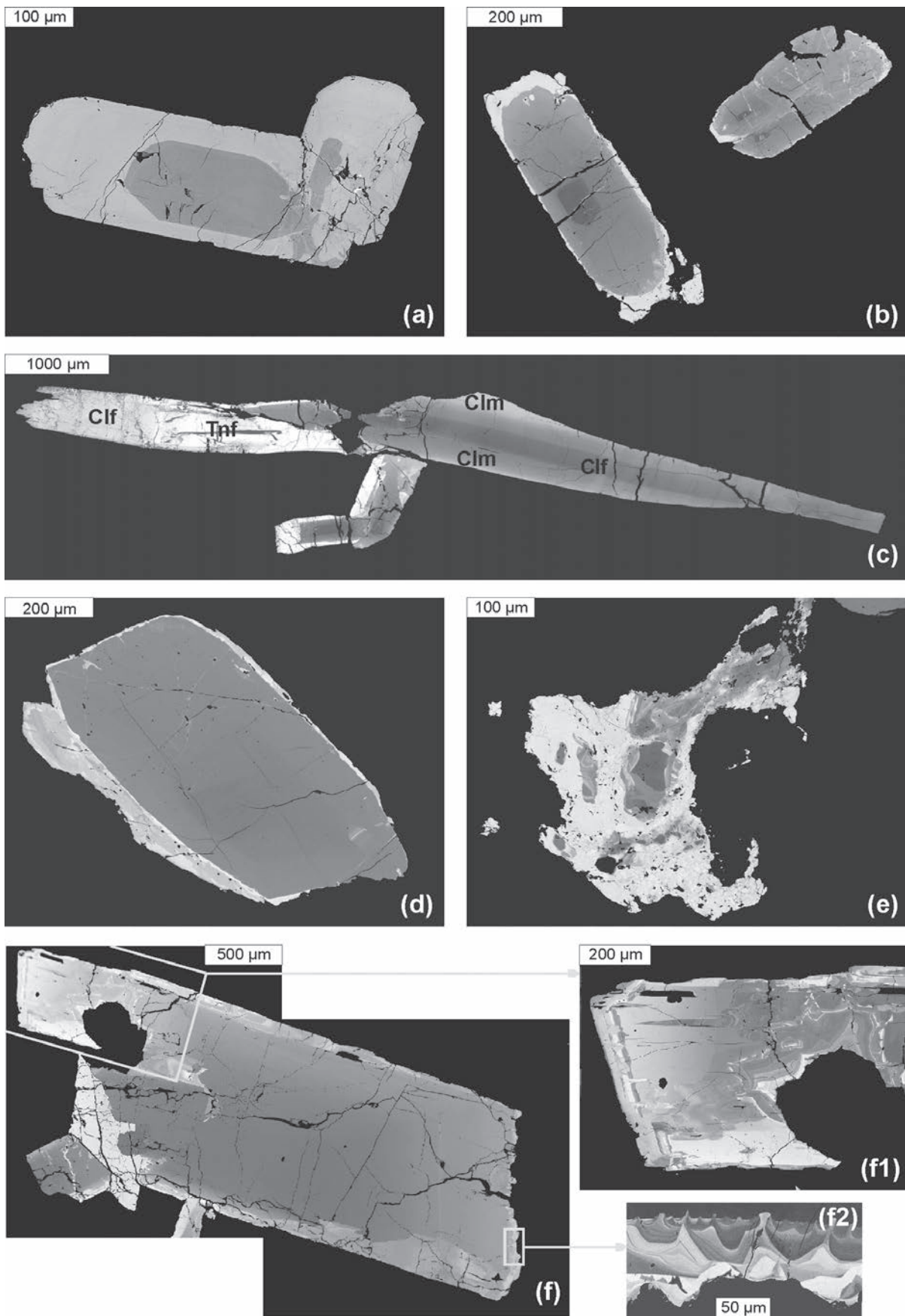
Tab. 1b Representative compositions of a columbite crystal of fractionation style I+IIb

| P114a	1	2	3	4	5	6	7	8	9	10	11	12	13	14	15
							wt. %								
WO_3	0.58	0.40	0.28	0.46	0.48	0.55	0.46	0.42	0.07	0.43	0.42	0.45	0.15	0.31	0.28
Nb_2O_5	64.13	62.51	59.08	55.76	53.16	49.64	47.40	44.35	40.51	37.89	33.90	30.46	27.64	27.42	29.74
Ta_2O_5	15.85	17.41	21.17	24.28	26.49	30.16	32.90	35.97	40.75	42.94	47.14	51.34	54.21	54.01	51.65
TiO_2	0.72	0.73	0.65	0.68	0.75	0.72	0.61	0.62	0.89	0.78	0.66	0.69	0.46	0.72	0.87
ZrO_2	0.00	0.00	0.00	0.12	0.10	0.17	0.14	0.12	0.14	0.17	0.15	0.00	0.00	0.00	0.00
SnO_2	0.18	0.27	0.24	0.29	0.33	0.32	0.27	0.40	0.36	0.40	0.45	0.40	0.18	0.29	0.39
Sc_2O_3	0.00	0.04	0.03	0.05	0.06	0.06	0.06	0.06	0.09	0.07	0.12	0.10	0.14	0.12	0.11
Fe_2O_3	0.00	0.00	0.00	0.00	0.00	0.00	0.00	0.15	0.00	0.00	0.15	0.00	0.50	0.47	0.97
FeO	9.84	9.66	9.30	9.05	9.01	8.88	8.94	8.79	8.84	9.01	9.10	9.43	9.45	10.44	11.40
MnO	8.95	9.38	9.48	9.47	9.27	8.99	9.09	8.96	8.21	8.18	7.63	7.08	6.50	5.51	4.52
MgO	0.00	0.00	0.00	0.00	0.00	0.00	0.00	0.00	0.00	0.00	0.00	0.00	0.00	0.00	0.03
Total	100.26	100.40	100.23	100.16	99.65	99.49	99.87	99.85	99.86	99.86	99.71	99.95	99.23	99.28	99.96
					Content of ions on the basis of 24 O and 12 cations pfu										
Fe^{2+}	1.961	1.935	1.896	1.875	1.896	1.904	1.933	1.929	1.976	2.042	2.110	2.226	2.279	2.513	2.685
Mn^{2+}	1.806	1.903	1.959	1.987	1.976	1.950	1.991	1.991	1.860	1.877	1.792	1.693	1.589	1.343	1.078
Mg^{2+}	0.000	0.000	0.000	0.000	0.000	0.000	0.000	0.000	0.000	0.000	0.000	0.000	0.000	0.000	0.011
Sc^{3+}	0,000	0,009	0,007	0,011	0,012	0,014	0,014	0,015	0,021	0,018	0,029	0,025	0,035	0,031	0,028
ΣA	*3.767*	*3.847*	*3.862*	*3.873*	*3.884*	*3.868*	*3.937*	*3.935*	*3.856*	*3.937*	*3.930*	*3.943*	*3.903*	*3.888*	*3.803*
W^{6+}	0.036	0.025	0.018	0.029	0.031	0.037	0.031	0.029	0.005	0.030	0.030	0.033	0.011	0.023	0.021
Nb^{5+}	1.027	1.134	1.404	1.635	1.812	2.102	2.313	2.566	2.963	3.164	3.553	3.940	4.252	4.229	3.956
Ta^{5+}	6.906	6.769	6.514	6.243	6.045	5.750	5.541	5.261	4.896	4.642	4.248	3.885	3.605	3.570	3.787
Ti^{4+}	0.129	0.131	0.119	0.127	0.141	0.138	0.118	0.123	0.178	0.158	0.138	0.146	0.099	0.155	0.185
Zr^{4+}	0.000	0.000	0.000	0.015	0.013	0.022	0.018	0.015	0.019	0.022	0.020	0.000	0.000	0.000	0.000
Sn^{4+}	0.017	0.026	0.023	0.028	0.033	0.033	0.028	0.042	0.038	0.044	0.049	0.045	0.021	0.033	0.043
Fe^{3+}	0,000	0,000	0,000	0,000	0,000	0,000	0,000	0,029	0,000	0,000	0,031	0,000	0,108	0,101	0,206
ΣB	*8.115*	*8.086*	*8.079*	*8.077*	*8.075*	*8.081*	*8.049*	*8.065*	*8.099*	*8.061*	*8.070*	*8.049*	*8.097*	*8.112*	*8.197*
O^{2-}	24	24	24	24	24	24	24	24	24	24	24	24	24	24	24
Mn/(Mn+Fe)	*0.479*	*0.496*	*0.508*	*0.515*	*0.510*	*0.506*	*0.507*	*0.504*	*0.485*	*0.479*	*0.456*	*0.432*	*0.400*	*0.339*	*0.272*
Ta/(Ta+Nb)	*0.129*	*0.144*	*0.177*	*0.208*	*0.231*	*0.268*	*0.295*	*0.328*	*0.377*	*0.405*	*0.455*	*0.503*	*0.541*	*0.542*	*0.511*

within the blocky feldspar zone. It is usually coupled with a sudden decrease in the Mn/(Mn + Fe) ratio at almost constant Ta/(Ta + Nb) values (trend IIa in Fig. 3a) and occasionally with a distinct progressive decrease in Mn/(Mn + Fe) at increasing Ta/(Ta + Nb) values (trend IIb in Fig. 3b). Columbite-group minerals that occur together with zircon, monazite, thorite and fergusonite close to the border of the graphic and blocky feldspar zones display only a slight progressive Mn–Fe fractionation as well as Ta increase during the reversed Mn–Fe fractionation.

⇦

Fig. 2 Back-scattered electron (BSE) images of columbite-group minerals: **a** – a two-zone crystal of columbite-(Fe) of fractionation style IIc (P123d specimen); **b** – a crystal of columbite-(Fe) overgrown by younger columbite-(Fe) with higher Ta, fractionation style IIa (P121c specimen); **c** – a crystal of columbite-(Fe) evolving progressively to columbite-(Mn), intergrown with tantalite-(Fe) evolving to columbite-(Fe); fractionation style IIa (P41 specimen); **d** – a crystal of columbite-(Fe) overgrown by younger, heterogeneous columbite-(Fe) with higher Ta; fractionation style IIa (P117 specimen); **e** – replacement of columbite-(Fe) by younger columbite-(Fe) with higher Ta; fractionation style IIa (P118b specimen); **f** – a crystal of columbite-(Fe) evolving progressively to tantalite-(Fe); fractionation style IIb (P114a specimen); inserts f1 and f2 present details of compositional heterogeneity that indicates oscillations in Mn–Fe and Ta–Nb activities. Abbreviations: Clf – columbite-(Fe), Clm – columbite-(Mn), Tnf – tantalite-(Fe).

Nonetheless, the reversed Mn–Fe fractionation attains almost the same degree (trend IIc in Fig. 3c) as in crystals showing trends IIa and IIb.

The progressive Mn–Fe fractionation of trend I is typically connected with decreasing Fe, Ti, Sn and Sc contents in columbite growing under reducing conditions ($Fe^{3+}/Fe_{total} \approx 0$). The nature of the reversed fractionation trends IIa–c results from the opposite tendencies, with distinct enrichment in Ti, Sn, Sc and sometimes also Zr and Fe under increasing Fe^{3+}/Fe_{total} ratios, especially at the final stages of crystallization (Tabs 1a–c). Generally, many CGM with Mn/(Mn + Fe) ratios below ~0.35, and thus related to the final stages of the reversed Mn–Fe fractionation, show distinct enrichment in Ti, and sometimes also Sc, followed by higher Sn values (Fig. 4). Titanium commonly concentrates in the outermost zones of the CGM crystals formed at usually Mn/(Mn + Fe) ≤ 0.20, and sporadically in CGM inclusions occurring in ishikawaite crystals, reaching similar TiO_2 contents of *c*. 3.13 wt. % (0.58–0.59 Ti *apfu*). Tin concentrated with, or without, Ti at the final stages of CGM crystallization, reaching the highest SnO_2 content, 3.14 wt. % (0.35 Sn *apfu*), in tantalite-(Fe) (Fig. 2e; Tab. 1a).
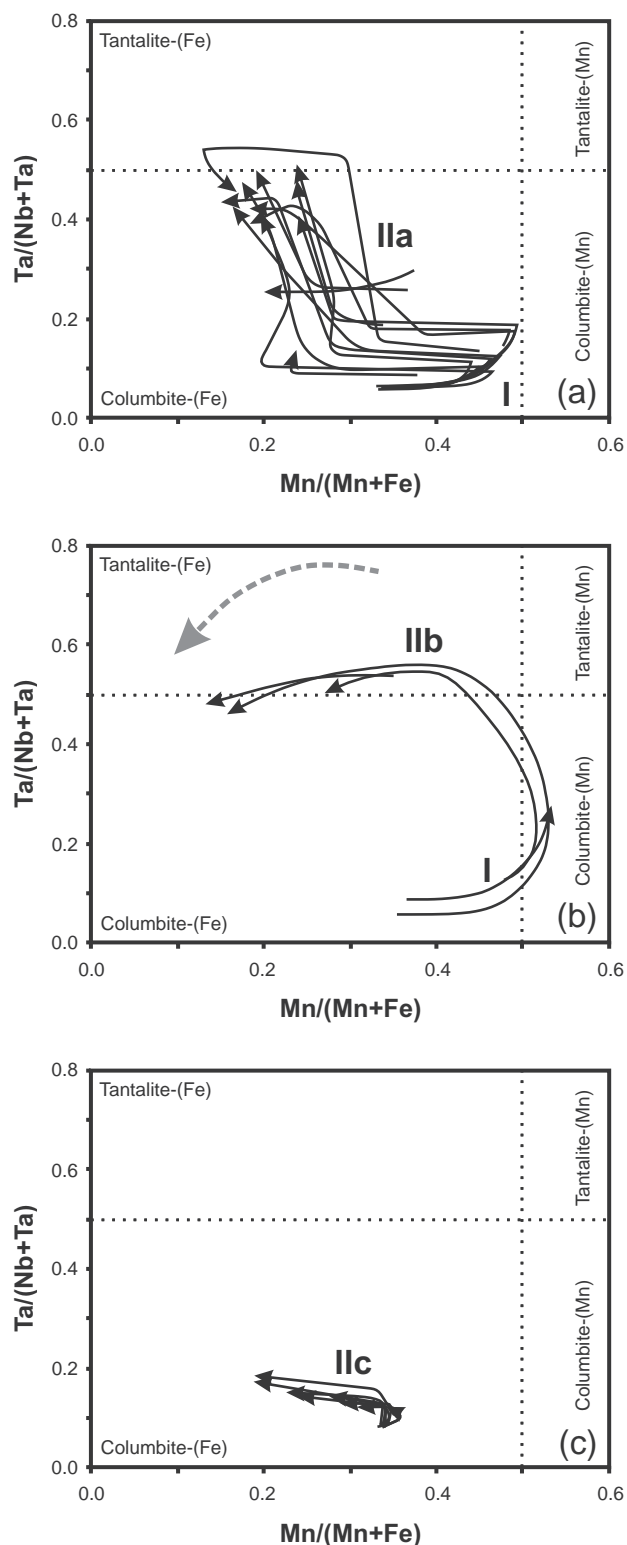
Fig. 3 Ta–Nb vs. Mn–Fe fractionation paths for CGM in the columbite quadrilateral: **a** – typical paths with suddenly reversed Mn–Fe fractionation; **b** – paths with possibly continuous crystallization with distinct reversed Mn–Fe fractionation at increasing Ta–Nb fractionation; grey dashed line – fractionation path of ferrowodginite; **c** – paths with negligible Ta–Nb fractionation at reversed Mn–Fe fractionation. I, IIa, IIb and IIc – styles of Ta–Nb vs. Mn–Fe fractionation.
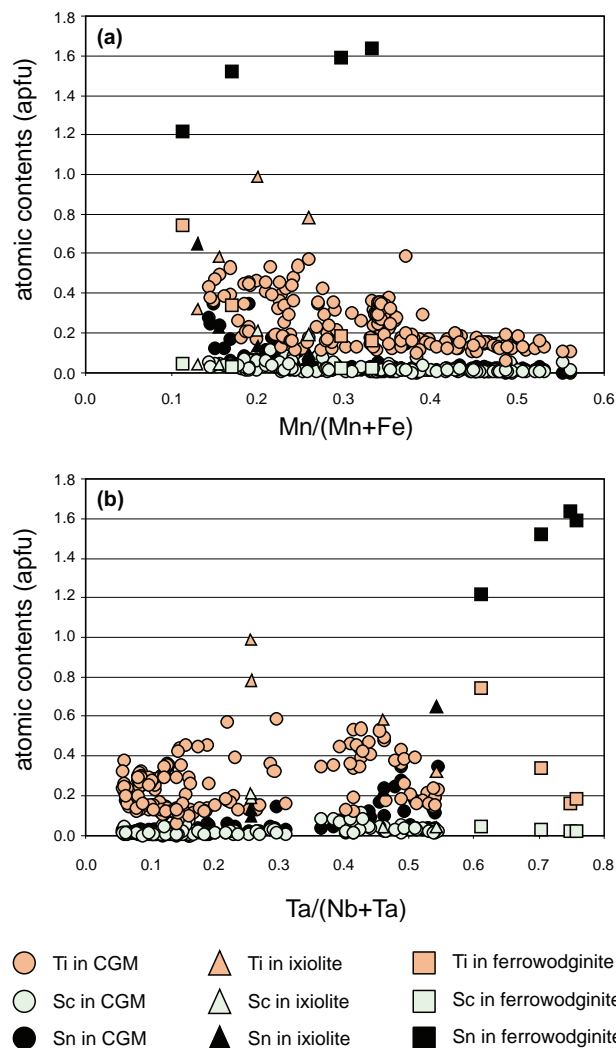
Fig. 4 Binary plots of atomic content of Ti, Sc and Sn vs. Mn–Fe fractionation expressed as Mn/(Mn + Fe) (**a**) and Ta–Nb fractionation expressed as Ta/(Nb + Ta) (**b**).

Scandium and Zr are subordinate; both components sometimes concentrate along with Ti. The greatest Sc_2O_3 content, 0.85 wt. % (0.18 Sc *apfu*), and ZrO_2 up to 0.45 wt. % (0.05 Zr *apfu*) were noted in titanian columbite. Finally, it is noteworthy that Mg is only a subordinate component, occasionally reaching 0.17 MgO wt. %, i.e. 0.06 Mg *apfu*, in the outermost zones of some columbite crystals.

The $(Nb + Ta + W) - (Ti + Sn + Zr + Hf) - (Fe_{total} + Mn + Mg + Sc)$ ternary diagram (Fig. 5) shows that the compositional trend of CGM runs from columbite–tantalite towards a hypothetical composition of $(Fe,Mn)_4(Ti,Sn)_4(Nb,Ta)_4O_{24}$, which can be obtained from CGM through the *euxenite-type* substitution $(Fe,Mn)^{2+} + (Nb,Ta)^{5+} \leftrightarrow (Sn,Fe)^{3+} + (Ti,Sn)^{4+}$, corroborated by a very strong negative correlation between the totals of $R^{2+}R^{5+}$ and $R^{3+}R^{4+}$ cations (Fig. 6a). This substitution was suggested for CGM and ixiolite by Novák

Tab. 1c Representative compositions of a columbite crystal of fractionation style IIc

| P124d	1	2	3	4
		wt. %		
WO_3	0.91	0.95	1.18	1.23
Nb_2O_5	67.23	61.09	59.64	57.95
Ta_2O_5	9.69	14.68	17.07	17.65
TiO_2	1.58	1.97	2.00	2.54
ZrO_2	0.00	0.37	0.00	0.00
SnO_2	0.21	0.37	0.32	0.31
Sc_2O_3	0.09	0.08	0.27	0.25
Fe_2O_3	0.61	1.55	0.66	1.45
FeO	12.78	11.66	13.17	13.66
MnO	6.74	6.64	5.46	4.28
MgO	0.06	0.04	0.07	0.08
Total	99.90	99.41	99.85	99.40
	Content of ions based on 24 O and 12 cations pfu			
Fe^{2+}	2.487	2.325	2.642	2.751
Mn^{2+}	1.329	1.340	1.110	0.873
Mg^{2+}	0.020	0.014	0.023	0.028
Sc^{3+}	0.018	0.016	0.057	0.052
ΣA	*3.854*	*3.696*	*3.833*	*3.704*
W^{6+}	0.055	0.059	0.073	0.077
Nb^{5+}	7.074	6.584	6.469	6.309
Ta^{5+}	0.613	0.952	1.114	1.156
Ti^{4+}	0.278	0.353	0.361	0.461
Zr^{4+}	0.000	0.043	0.000	0.000
Sn^{4+}	0.020	0.035	0.030	0.030
Fe^{3+}	0.107	0.279	0.120	0.263
ΣB	*8.146*	*8.304*	*8.167*	*8.296*
O^{2-}	24	24	24	24
Mn/(Mn+Fe)	*0.339*	*0.340*	*0.287*	*0.225*
Ta/(Ta+Nb)	*0.080*	*0.126*	*0.147*	*0.155*

and Čech (1996) with Wise et al. (1998) and confirmed recently by Beurlen et al. (2007).

4.2. Ixiolite

Both titanian ixiolite and stannian ixiolite are present in the Julianna pegmatites.

Titanian ixiolite has been found along with titanian columbite-(Fe) as irregular or elongated thin inclusions, up to 200 μm long, in crystals of ishikawaite hosted by quartz and associated with microcline, yellowish beryl and zircon, in the outermost part of the massive feldspars zone (Fig. 7a).

Fig. 5 Ternary diagram (Ti + Zr + Sn + Hf) – (Nb + Ta + W) – (Fe$_{total}$ + Mg + Mn + Sc) with compositions of CGM, ixiolite, ferrowodginite and cassiterite.
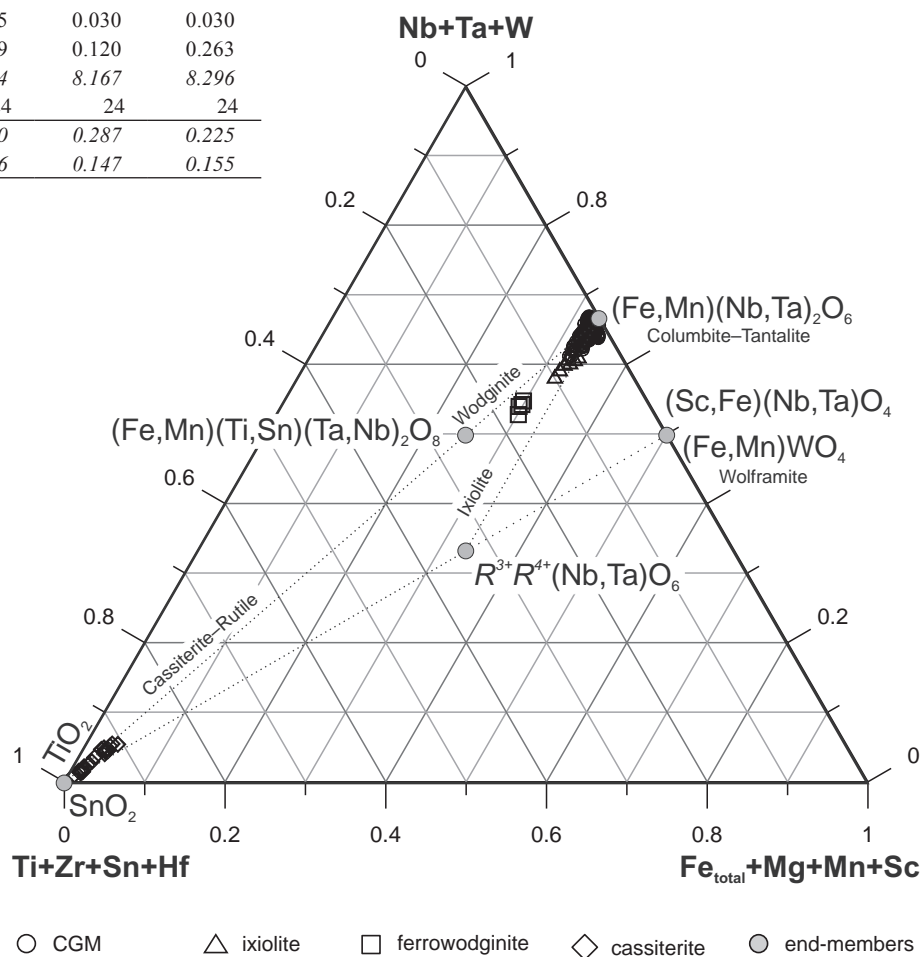
Columbite-(Fe) usually forms the cores of such inclusions, overgrown by thin rims of titanian ixiolite. This succession reflects the progressive *euxenite-type* substitution that brings three- and four-valent cations into the structure of a Fe- and Nb-bearing orthorhombic phase. Compared to CGM, the ixiolite shows a distinct enrichment in TiO_2 (up to 5.33 wt. %), Sc_2O_3 (to 1.0 wt. %) and rather low contents of SnO_2 (1.36 wt. %) as well as of calculated Fe_2O_3 (1.61 wt. %) (Tab. 2).

Stannian ixiolite (Fig. 7b) has been found in a grain composed of a relict of columbite-(Fe) with the reversed Mn–Fe fractionation of trend IIa. The relict is overgrown by titanian tantalite-(Fe), followed by stannian tantalite-(Fe) and again by titanian columbite-(Fe). Such a compositional evolution corresponds to the observation that the Ti enrichment in CGM precedes the increase of Sn. The appearance of titanian columbite-(Fe) at the final stage of crystal growth suggests that the high activity of Sn (5.73 wt. % of SnO_2 in the stannian ixiolite) was rather ephemeral. TiO_2 concentrations rise across the crystal from 1.09 wt. % in the tantalite-(Fe) to 1.50 wt. % in the stannian ixiolite, and reach 2.61 wt. % in titanian columbite-(Fe) (Tab. 2). Scandium does not concentrate in the minerals
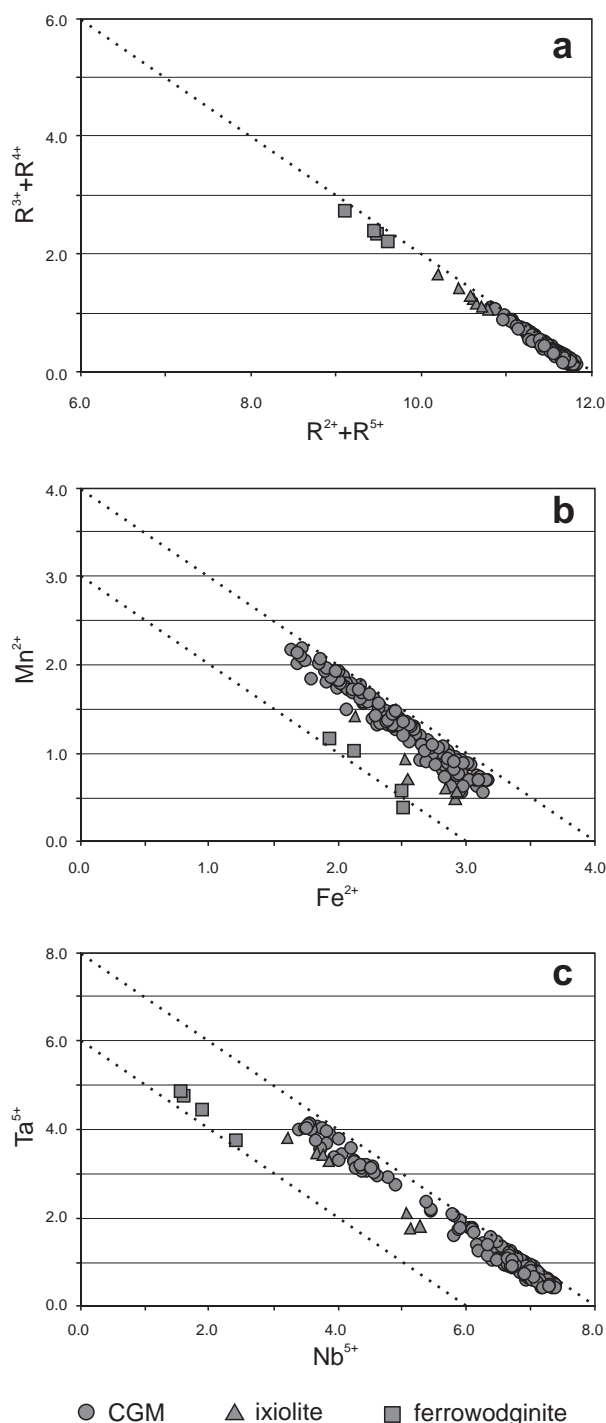
Fig. 6 Binary plots illustrating compositional relationships in CGM, ixiolite and ferrowodginite: **a** –$\Sigma(R^{3+} + R^{4+})$ vs. $\Sigma(R^{2+} + R^{5+})$; **b** – Mn^{2+} vs. Fe^{2+}; c) Ta^{5+} vs. Nb^{5+}. Dotted lines 4.0–4.0 and 3.0–3.0 in (b) and 8.0–8.0 and 6.0–6.0 in (c) denote the respective amounts of R^{2+} cations in ideal CGM and ferrowodginite, and R^{5+} cations in the same end-members, respectively.

forming this grain, whereas the calculated contents of Fe^{3+} are clearly elevated in the tantalite-(Fe), stannian ixiolite and columbite-(Fe) as well.

4.3. Ferrowodginite

One grain of Nb–Ti oxide 2 mm across contains a zone whose composition corresponds to ferrowodginite. The grain is composed of a crystal of columbite-(Fe) evolving to columbite-(Mn) and finally to tantalite-(Fe), partly corroded and overgrown by ferrowodginite and cassiterite (Fig. 7c; Tab. 2). The highest primary TiO_2 concentration found in the columbite-(Fe) core (1.90 wt. %) decreases along with Sn and Sc contents, finally reaching ~0.7 wt. % TiO_2 and ~0.3 wt. % SnO_2 in the outermost zone. On the other hand, Ta increases, relative to Nb, from Ta/(Ta + Nb) = 0.06 up to 0.54 at decreasing Mn/(Mn + Fe) ratios in the outermost zones of the columbite core. A younger titanian tantalite-(Fe) that, along with ferrowodginite, overgrows the columbite core of the grain shows TiO_2 and SnO_2 contents a magnitude higher, ranging from 1.1–1.2 wt. % to slightly less than 2.0 wt. % at almost the same Ta/(Ta + Nb) values. Ferrowodginite that co-crystallized with the tantalite shows progressively increasing TiO_2, reaching 3.49 wt. % at an almost constant SnO_2 content of 13.0 wt. % and Sn/(Sn + Ti) and Ta/(Ta + Nb) ratios decreasing from 0.91 to 0.82 and from 0.76 to 0.70, respectively. In the outermost zone, SnO_2 falls to 10.8 wt. % and the ratios to 0.61–0.62. The latest generation of ferrowodginite is overgrown by cassiterite, and in places contains small exsolutions of titanian ixiolite, with still more decreased Sn/(Sn + Ti) ratio down to 0.43 in the last mineral. The Mn–Fe and Ta–Nb fractionation path for the ferrowoodginite is almost parallel to that of tantalite-(Fe) evolving to titanian ixiolite (Fig. 3b). In the successive zones, the composition of ferrowodginite changes from: $(Fe^{2+}_{0.64}Mn_{0.39})_{\Sigma=1.03}(Sn_{0.55}Ta_{0.17}Fe^{3+}_{0.15}Ti_{0.06}Zr_{0.03}Sc_{0.01})_{\Sigma=0.97}(Ta_{1.42}Nb_{0.53}W_{0.05})_{\Sigma=2.00}O_8$ through: $(Fe^{2+}_{0.71}Mn_{0.35})_{\Sigma=1.06}(Sn_{0.53}Ta_{0.19}Fe^{3+}_{0.12}Ti_{0.06}Zr_{0.02}Sc_{0.01})_{\Sigma=0.94}(Ta_{1.43}Nb_{0.52}W_{0.05})_{\Sigma=2.00}O_8$ to $(Fe^{2+}_{0.83}Mn_{0.20})_{\Sigma=1.03}(Sn_{0.51}Ti_{0.17}Fe^{3+}_{0.14}Ta_{0.11}Zr_{0.03}Sc_{0.01})_{\Sigma=0.97}(Ta_{1.32}Nb_{0.63}W_{0.05})_{\Sigma=2.00}O_8$, and finally to $(Fe^{2+}_{0.83}Mn_{0.13})_{\Sigma=0.97}(Sn_{0.41}Ti_{0.25}Fe^{3+}_{0.22}Ta_{0.11}Zr_{0.02}Sc_{0.02})_{\Sigma=1.03}(Ta_{1.14}Nb_{0.81}W_{0.05})_{\Sigma=2.00}O_8$, with distinct increase in Nb, Ti, Fe^{3+} and Fe^{2+} and decrease in Ta, Sn and Mn. Titanium correlates negatively with Sn (Fig. 4b). The contents of $R^{2+}(Fe^{2+},Mn^{2+})$ and $R^{5+}(Ta^{5+},Nb^{5+})$ cations (3.0 and 6.0 *apfu*, respectively) are distinctly lower than in the associated columbite–tantalite and ixiolite crystals, being consistent with the formula of ferrowodginite (Figs 6b–c).

4.4. Pyrochlore-supergroup minerals

Pyrochlore-supergroup minerals are rarely found as alteration products covering or penetrating crystals of CGM, ixiolite and ferrowodginite (Figs 7c–e). They are represented by hydroxy- or keno-microlite with Ta/(Ta + Nb) = 0.78, and more frequently by zero-valent-dominant microlite with Ta/(Ta + Nb) ≈ 0.80–0.70, Pb-enriched zero-valent-dominant microlite with Ta/(Ta + Nb) ≈
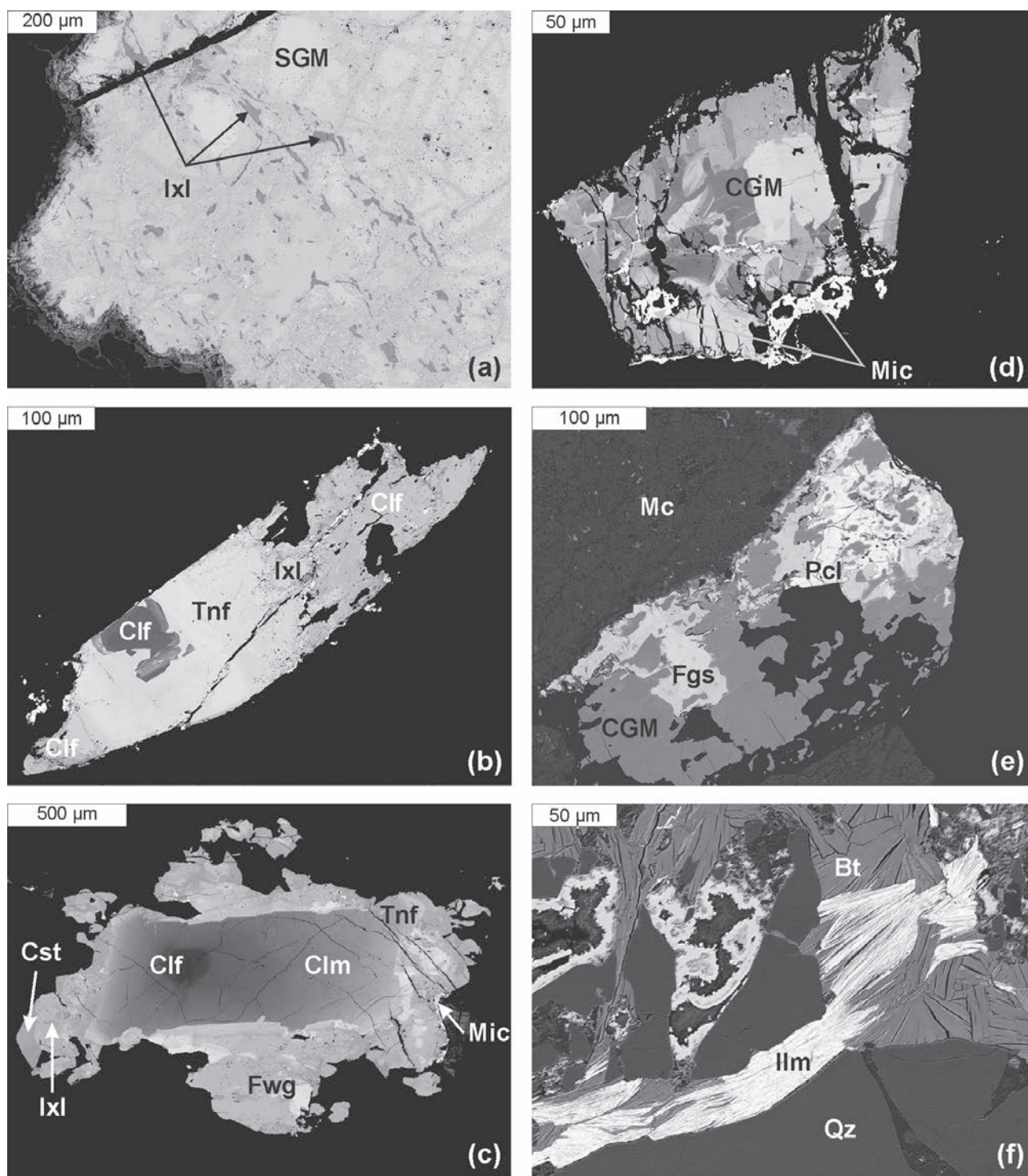
Fig. 7 Back-scattered electron (BSE) images: **a** – relics of titanian ixiolite in ishikawaite (P7 specimen); **b** – columbite-(Fe) replaced by titanian tantalite-(Fe) and stannian ixiolite (P116a specimen); **c** – a crystal of columbite-(Fe)–columbite-(Mn)–tantalite-(Fe) replaced by ferrowodginite and cassiterite (P13 specimen); **d** – microlite replacing columbite-group minerals (P119 specimen); **e** – Bi-rich pyrochlore associated with columbite-(Fe)–columbite-(Mn) and fergusonite-(Y) (P123 specimen); **f** – zincian ilmenite (P115 specimen). Abbreviations: Bt – biotite, Clf – columbite-(Fe), Clm – columbite-(Mn), CGM – columbite-group minerals, Cst – cassiterite, Fgs – fergusonite, Fwg – ferrowodginite, Ilm – ilmenite, Ixl – ixiolite, Mc – microcline, Mic – microlite, Pcl – pyrochlore, Qz – quartz, SGM – samarskite-group minerals, Tnf – tantalite-(Fe).

0.88–0.68, Bi-enriched zero-valent-dominant pyrochlore with Ta/(Ta + Nb) = 0.42, and hydroxy- or keno-, Bi-rich

pyrochlore with the ratio ranging from 0.17 to 0.07; the Mn/(Mn + Fe) ratio is always close to zero (Tab. 3). The

Tab. 2 Representative compositions of ixiolite and ferrowodginite

	P7/1	P7/2	P7/3	P13/10	P41/13	P116a	P13/11	P13/12	P13/13	P13/14
	Ixl	Ixl	Ixl	Ixl	Ixl	Ixl	Fwg	Fwg	Fwg	Fwg
					wt. %					
WO_3	2.16	2.20	1.99	1.78	2.39	1.64	1.98	1.98	2.02	2.25
Nb_2O_5	44.45	47.23	46.04	31.39	29.20	24.94	11.56	11.18	13.89	18.81
Ta_2O_5	30.92	27.07	26.25	44.31	45.96	49.10	57.30	58.11	56.64	48.78
TiO_2	3.13	4.21	5.33	2.85	2.07	1.50	0.73	0.80	1.51	3.49
ZrO_2	0.45	0.25	0.30	0.00	0.00	0.36	0.56	0.39	0.61	0.47
SnO_2	1.50	0.93	1.36	2.07	2.50	5.73	13.46	12.98	12.74	10.80
Sc_2O_3	0.06	0.89	1.00	0.16	0.22	0.15	0.09	0.08	0.11	0.19
Fe_2O_3	1.38	0.79	1.61	2.16	1.96	1.76	1.94	1.60	1.90	3.08
FeO	10.12	12.21	12.34	12.48	12.62	12.22	7.53	8.24	9.91	10.51
MnO	6.62	4.46	3.39	2.62	2.34	2.04	4.54	4.00	2.34	1.65
MgO	0.13	0.17	0.17	0.03	0.06	0.05	0.00	0.02	0.04	0.02
Total	100.93	100.41	99.77	99.85	99.34	99.46	99.69	99.38	99.72	100.07
				Content of ions on the basis of 24 O and 12 cations						
W^{6+}	0.141	0.141	0.127	0.126	0.172	0.121	0.157	0.158	0.157	0.166
Nb^{5+}	5.067	5.277	5.129	3.858	3.668	3.213	1.600	1.558	1.882	2.417
Ta^{5+}	2.120	1.819	1.759	3.276	3.473	3.806	4.771	4.873	4.454	3.770
Ti^{4+}	0.594	0.783	0.989	0.584	0.433	0.322	0.167	0.186	0.341	0.746
Zr^{4+}	0.055	0.030	0.036	0.000	0.000	0.049	0.084	0.059	0.089	0.065
Sn^{4+}	0.151	0.092	0.133	0.442	0.277	0.651	1.643	1.595	1.522	1.224
Sc^{3+}	0.013	0.192	0.214	0.039	0.054	0.037	0.025	0.023	0.029	0.046
Fe^{3+}	0.262	0.147	0.299	0.225	0.410	0.377	0.448	0.372	0.429	0.660
Fe^{2+}	2.134	2.524	2.542	2.837	2.931	2.912	1,929	2.125	2.485	2.499
Mn^{2+}	1.413	0.933	0.708	0.604	0.555	0.492	1.177	1.044	0.595	0.397
Mg^{2+}	0.051	0.062	0.064	0.011	0.025	0.020	0.000	0.008	0.016	0.010
Σ cations	12.000	12.000	12.000	12.000	12.000	12.000	12.000	12.000	12.000	12.000
O^{2-}	24	24	24	24	24	24	24	24	24	24
Mn/(Mn+Fe)	0.371	0.259	0.200	0.156	0.143	0.130	0.331	0.295	0.169	0.112
Ta/(Ta+Nb)	0.295	0.256	0.255	0.459	0.486	0.542	0.749	0.758	0.703	0.609

Abbreviations: Ixl - ixiolite, Fwg - ferrowodginite.

content of F commonly is below detection limit; Ti, Sn and U generally decrease along with Ta/(Ta + Nb) and reach their lowest contents in Bi-rich pyrochlore. On the other hand, the pyrochlore has the highest Fe_2O_3 content, even up to 7.3 wt. %.

4.5. Cassiterite

Cassiterite is an accessory component, associated spatially with tantalite-(Fe) or ferrowodginite (Fig. 2, Fig. 7). It usually forms small grains but a crystal 1 cm in size was also found. Ta_2O_5 exceeds Nb_2O_5 in all analyzed crystals, reaching commonly 5.4–5.5 wt. % and even 6.4 wt. % in cassiterite intergrown with ferrowodginite. Nb_2O_5 is usually below 1.0 wt. % (Tab. 4). The cassiterite adjoining tantalite shows a progressive Ta enrichment expressed in increasing Ta/(Ta + Nb) from 0.50 to 0.81, whereas the opposite trend of Ta/(Ta + Nb), decreasing from 0.84 to 0.81, was found in the crystal accompanied by ferro-wodginite. In the ternary (Ti + Zr + Sn + Hf)–(Nb + Ta + W)–(Fe_{total} + Mg + Mn + Sc) diagram cassiterite compositions plot along the cassiterite – columbite–tantalite tie line (Fig. 5). This suggests the dominant replacement

$R^{2+}(Fe^{2+},Mg^{2+}) + 2\ R^{5+}(Ta^{5+},Nb^{5+}) \rightarrow 3\ Sn^{4+}$, typical of cassiterite in many pegmatites worldwide.

4.6. Ilmenite-group minerals

Sporadic ilmenite and pyrophanite crystals are usually present as inclusions of micrometer scale (Fig. 7f) and scarcely reach 1 cm. Their chemical compositions (Tab. 5) vary from typical ilmenite with Mn/(Mn + Fe) = 0.06 found in outer parts of the blocky feldspars zone to typical pyrophanite with Mn/(Mn + Fe) = 0.82–0.83 in axial parts of the massive feldspar zone. Both minerals contain only subordinate Nb and Ta ($\leq$ 2.57 wt. % of Nb_2O_5 and 1.02 wt. % of Ta_2O_5), always with Nb_2O_5 exceeding Ta_2O_5. The ilmenite is devoid of Zn, although all other inclusions of the ilmenite-group minerals have ZnO up to 9.50 wt. %.

5. Associated ferromagnesian phases

5.1. Biotite

Biotite is a subordinate to accessory constituent and forms: (i) medium- to coarse-grained platy crystals in the

Tab. 3 Representative compositions of pyrochlore-supergroup minerals

|	P13/a	P13/b	109/a	109/b	P119a	P119b	P121a	P120
				wt. %				
WO_3	0.00	0.82	0.77	1.29	0.00	0.77	0.00	0.66
Nb_2O_5	8.79	10.31	10.71	4.30	13.10	12.14	12.32	23.94
Ta_2O_5	58.72	57.79	62.76	53.67	52.82	42.79	54.82	8.38
SiO_2	0.44	0.99	0.27	1.42	0.34	1.62	0.21	2.83
TiO_2	2.23	1.89	1.55	2.54	3.49	3.10	3.26	1.67
ZrO_2	0.09	0.00	0.00	0.00	0.00	0.25	0.07	0.66
SnO_2	1.58	1.54	1.56	1.30	1.62	0.86	1.79	0.11
ThO_2	0.26	0.47	0.00	0.00	0.12	0.10	0.00	0.00
UO_2	8.88	6.54	0.00	5.05	12.10	10.58	12.18	6.80
Al_2O_3	0.00	0.00	0.00	0.04	0.00	0.71	0.10	0.50
Fe_2O_3	3.09	1.13	0.00	2.10	1.23	2.35	2.51	7.33
Sc_2O_3	0.11	0.11	0.00	0.00	0.12	0.11	0.06	0.04
La_2O_3	0.00	0.00	0.00	0.00	0.00	0.00	0.00	0.27
Ce_2O_3	0.42	0.44	0.00	0.00	0.13	0.27	0.44	0.58
Bi_2O_3	0.00	0.00	0.00	0.00	0.00	0.00	0.00	23,96
MnO	0.10	0.06	0.25	0.08	0.10	0.13	0.00	0.13
MgO	0.00	0.07	0.00	0.04	0.00	0.08	0.03	0.21
CaO	7.86	0.82	16.62	0.65	6.52	0.70	4.30	3.82
BaO	0.75	0.61	0.28	0.35	0.70	0.66	0.84	0.67
PbO	0.00	10.19	0.00	20.92	0.00	13.65	0.00	9.46
Na_2O	0.03	0.01	0.26	0.04	0.00	0.00	0.15	0.30
K_2O	0.06	0.01	0.00	0.00	0.12	0.05	0.04	0.08
H_2O*	0.75	1.79	1.31	1.28	0.70	0.66	0.84	0.95
F	0.00	0.00	0.80	0.00	0.00	0.00	0.00	0.00
$-O=F_2$			−0.34					
Total	94.15	95.58	96.80	95.07	93.03	92.51	94.80	93.36
Content of ions based on B (W + Nb + Ta + Ti + Zr + Sn + Al + Fe^{3+}) = 2 pfu								
W^{6+}	0.000	0.018	0.017	0.032	0.000	0.018	0.000	0.016
Nb^{5+}	0.323	0.397	0.405	0.186	0.484	0.483	0.434	1.031
Ta^{5+}	1.297	1.339	1.429	1.395	1.173	1.024	1.161	0.217
Ti^{4+}	0.136	0.121	0.097	0.183	0.215	0.205	0.191	0.120
Zr^{4+}	0.003	0.000	0.000	0.000	0.000	0.011	0.003	0.031
Sn^{4+}	0.051	0.052	0.052	0.050	0.053	0.030	0.056	0.004
Th^{4+}	0.005	0.009	0.000	0.000	0.002	0.002	0.000	0.000
U^{4+}	0.161	0.124	0.000	0.107	0.220	0.207	0.211	0.144
Al^{3+}	0.000	0.000	0.000	0.005	0.000	0.074	0.009	0.056
Fe^{3+}	0.189	0.072	0.000	0.151	0.076	0.156	0.147	0.526
Sc^{3+}	0.007	0.008	0.000	0.000	0.008	0.008	0.004	0.004
La^{3+}	0.000	0.000	0.000	0.000	0.000	0.000	0.000	0.010
Ce^{3+}	0.012	0.014	0.000	0.000	0.004	0.009	0.013	0.020
Bi^{3+}	0.000	0.000	0.000	0.000	0.000	0.000	0.000	0.588
Mn^{2+}	0.007	0.004	0.018	0.006	0.007	0.010	0.000	0.010
Mg^{2+}	0.000	0.009	0.000	0.006	0.000	0.010	0.003	0.030
Ca^{2+}	0.684	0.075	1.490	0.066	0.571	0.066	0.359	0.390
Ba^{2+}	0.024	0.020	0.009	0.013	0.022	0.023	0.026	0.025
Pb^{2+}	0.000	0.234	0.000	0.538	0.000	0.323	0.000	0.243
Na^+	0.005	0.002	0.042	0.008	0.000	0.000	0.023	0.054
K^+	0.006	0.001	0.000	0.000	0.012	0.006	0.004	0.009
O^{2-}	5.593	4.984	6.000	5.186	5.718	5.069	5.136	6.000
OH^-	0.407	1.016	0.733	0.814	0.282	0.931	0.864	0.601
F	0.000	0.000	0.211	0.000	0.000	0.000	0.000	0.000
ΣA	0.911	0.500	1.559	0.745	0.846	0.664	0.643	1.528
ΣB	2.000	2.000	2.000	2.000	2.000	2.000	2.000	2.000
Mn/(Mn+Fe)	0.035	0.055	1.000	0.039	0.083	0.058	0.000	0.019
Ta/(Ta+Nb)	0.801	0.771	0.779	0.882	0.708	0.679	0.728	0.174

granitic border zone, (ii) elongated lath-shaped crystals, up to 60 cm long, in the wall zone and graphic intermediate zone and (iii) thin giant plates that occur in the inner intermediate zone. Type (iii) is generally observed in the more primitive Julianna pegmatites and gives way to muscovite in the more evolved types. Biotite crystals of this type are often interleaved with muscovite that sometimes forms perfectly shaped pseudohexagonal plates. More random muscovitization of biotite is also common, particularly in the intermediate zones of the pegmatites. Chloritization is widespread. Titanite, ilmenite, rutile, apatite and zircon form common inclusions in biotite. Some of the titanite inclusions are euhedral to subhedral crystals distributed randomly within the biotite host. Others, however, are less regular, subhedral to anhedral, and are grouped along the cleavage planes of biotite. While the first type can represent primary titanite that crystallized simultaneously with biotite, the latter is rather a secondary exsolved titanite. There is no clear relation between the amount of exsolved titanite and the intensity of chloritization, suggesting that the two processes operated independently. The presence of exsolved titanite could indicate partial re-equilibration of biotite with the cooling pegmatite-forming melt. The analyzed biotites, sampled from the border and wall zones from three different pegmatites, are trioctahedral true micas, transitional between ferri- and magnesio-biotites (for the most part annite) and show Si from 5.46 to 5.65 *apfu*, ^{VI}Al from 0.22 to 0.66 *apfu* and Mg from 1.77 to 2.62 *apfu*. Moderate Ti (0.16–0.46 *apfu*) and low Mn (≤ 0.07 *apfu*), Ca (≤ 0.02 *apfu*), Na (≤ 0.09 *apfu*) and Ba (≤ 0.02 *apfu*) were found (Tab. 6, Fig. 8). The biotite compositions from individual veins show slight differences in Fe/(Fe + Mg) and octahedral Al, which may reflect various degree of fractionation between the pegmatites. Commonly the rims of biotite crystals show lower Ti and higher octahedral Al contents compared to the cores.

Tab. 4 Representative compositions of cassiterite

	P107	P107b	P114a	P114b	P114c	P13a	P13b	P13c
	wt. %							
WO_3	0.07	0.57	0.00	0.32	0.47	0.13	0.20	0.23
Nb_2O_5	0.77	0.78	0.83	1.10	0.92	0.58	0.77	0.93
Ta_2O_5	1.26	5.48	1.42	3.23	5.41	5.11	5.75	6.42
TiO_2	0.22	0.28	0.24	0.16	0.17	0.39	0.39	0.45
SnO_2	96.33	90.89	96.47	93.55	91.14	92.87	91.57	90.00
Fe_2O_3	0.38	0.00	0.45	0.06	0.00	0.79	0.52	1.17
FeO	0.13	1.07	0.06	0.80	1.04	0.54	0.85	0.72
MgO	0.07	0.06	0.11	0.05	0.09	0.08	0.07	0.07
Total	99.24	99.13	99.57	99.27	99.24	100.48	100.13	99.98
Content of ions on the basis of 24 O and 12 cations								
W^{6+}	0.006	0.045	0.000	0.025	0.037	0.010	0.016	0.018
Nb^{5+}	0.105	0.108	0.112	0.150	0.126	0.078	0.104	0.126
Ta^{5+}	0.104	0.453	0.116	0.266	0.447	0.415	0.470	0.523
Ti^{4+}	0.050	0.064	0.054	0.0376	0.038	0.087	0.089	0.100
Sn^{4+}	11.583	11.017	11.553	11.282	11.036	11.064	10.960	10.758
Fe^{3+}	0.087	0.000	0.102	0.014	0.000	0.177	0.118	0.264
Fe^{2+}	0.034	0.271	0.014	0.202	0.265	0.134	0.214	0.181
Mg^{2+}	0.033	0.028	0.049	0.024	0.042	0.034	0.030	0.030
$\Sigma cations$	12.000	11.987	12.000	12.000	11.992	12.000	12.000	12.000
O^{2-}	24	24	24	24	24	24	24	24
$Ta/(Ta+Nb)$	0.497	0.808	0.508	0.639	0.780	0.842	0.819	0.807

5.2. Tourmaline

Black to dark brown tourmaline is the most common accessory mineral associated with the CGM. It occurs as subhedral to euhedral crystals in the graphic intermediate zone up to the quartz core. Trigonal prisms of the tourmaline found in the Julianna-(4 + 5) dyke reached up to 70 cm in length and 7 cm in diameter (Szuszkiewicz et al. in print).

biotite 'P2'   biotite 'P3'   biotite 'T'
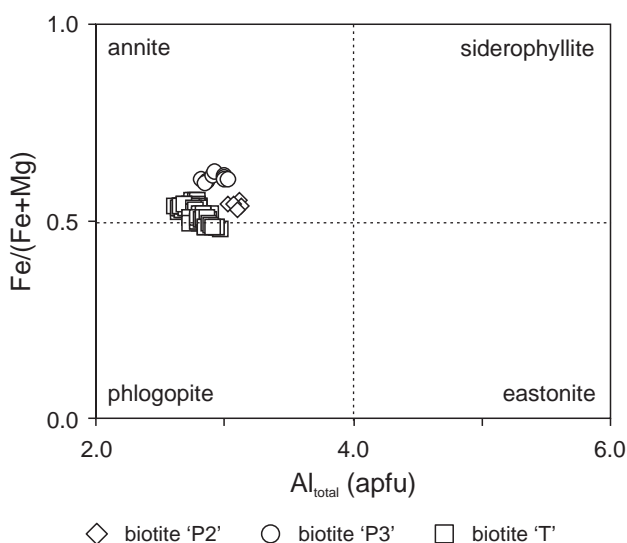
Fig. 8 Compositional plot of biotite in the phlogopite–annite–siderophyllite–eastonite system.

The tourmaline crystals are basically composed of two distinct zones (Fig. 9): (I) a core, showing pleochroism from dark blue / blue / bluish (ω) to colorless (ε), and (II) a mantle with pleochroism from olive-green / olive-brown / brownish, brown (ω) to colorless, sometimes with a delicate yellowish tint (ε). Representative chemical analyses of the two tourmaline generations (I and II), with additional subzones 'a' and 'b' in the core and mantle of crystals T1 and T2 from Fig. 9, are presented in Tab. 7 along with analyses of crystals P2 and P115. In the X-site vacancy–Ca–(Na + K) classification diagram the analyses plot in the field of the alkali tourmaline group, only occasionally passing into that of the X-vacant tourmaline group (Fig. 10a). Elevated Ca^{2+} contents were found only in the P115 tourmaline, adjacent to Ca-bearing minerals like titanite, epidote and zoisite. In the triangle ^YFe (Fe total as Fe^{2+})–^YAl –^YMg, all the tourmaline analyses form distinct clusters in different regions of the schorl field (Fig. 10b). Generally, almost all crystals show similar ^YAl contents. Taking into account relatively abundant vacancy at the X site, it can reflect the presence of the foitite and magnesiofoitite components. T2 and P115 crystals from internal parts of the pegmatites are distinctly enriched in Fe, whereas crystal T1, from a thin marginal vein, contains much more Mg. A group of analyses with higher Ca content (P115 tourmaline) plots generally along the line corresponding to the contents ~50 at. % ^YFe, which indicates a dominant Mg → Al replacement. The positive covariations ^XCa vs. ^YMg or $^Y(Mg + Fe)$ and negative ^XCa vs. ^YAl (each with a coefficient ~ 2.0) and ^XCa vs. X-site vacancy (~ 1.0) (Fig. 11) prove a significant role for the substitution $^XCa + 2^YMg^{2+} \rightarrow ^X\square + 2^YAl^{3+}$, with a small amount of $^YAl^{3+}$ replaced by Ti^{4+}.

Titanium is the only component that seems to correlate with the observed differences in tourmaline pleochroism. The bluish core (Ia in Tab. 7 and Fig. 9) has very low Ti^{4+} contents, from less than 0.005 to ~0.020 *apfu*, and low Mn/(Mn + Fe) ranging from *c.* 0.005 to slightly above 0.030 (Fig. 12). The outermost zone of

Fig. 9 Internal texture of tourmaline crystals in transverse sections: **a** – crystal T2 from an internal part of the Julianna dyke; **b** – crystals T1 from a peripheral pegmatite vein.
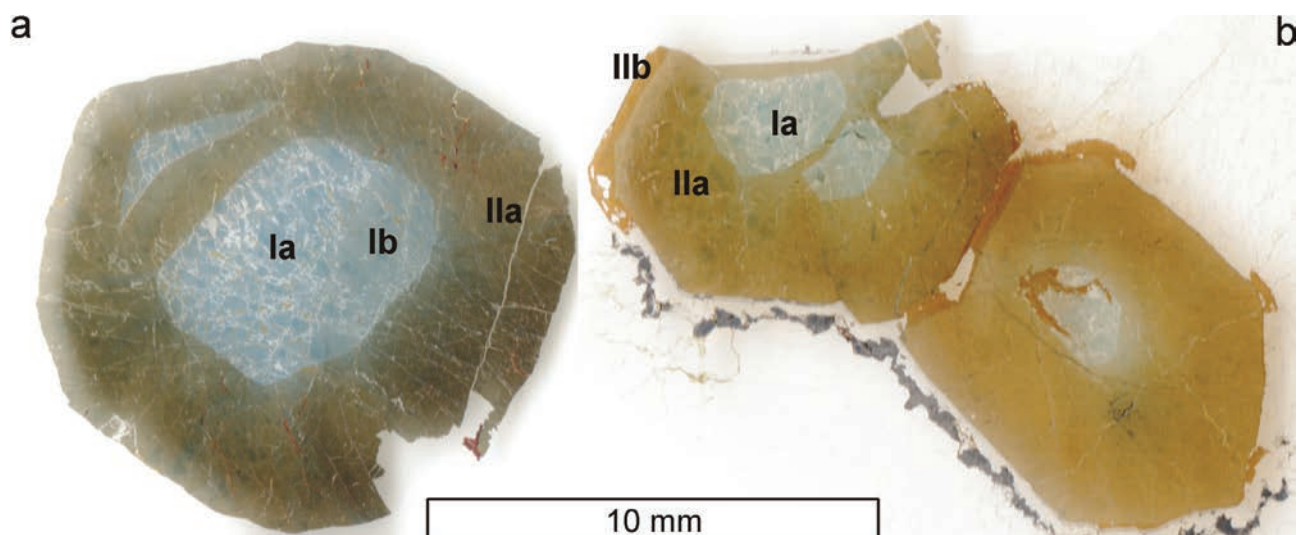
⇨

Tab. 5 Representative compositions of ilmenite-group minerals

	ES4a	P120a	P120b	P120c	P120d	P120e	P120f	P133
	Ilm	Ilm	Ilm	Ilm	Ilm	Ilm	Prf	Prf
				wt. %				
WO_3	0.00	0.00	0.00	0.00	0.00	0.00	0.00	0.38
Nb_2O_5	0.61	1.25	2.27	2.57	1.30	0.61	0.85	0.43
Ta_2O_5	0.30	0.30	1.02	0.75	0.16	0.18	0.18	0.00
TiO_2	51.23	51.24	49.31	51.20	52.32	51.30	50.65	51.48
Al_2O_3	0.00	0.00	0.23	0.00	0.00	0.04	0.18	0.00
Sc_2O_3	0.03	0.00	0.00	0.00	0.00	0.00	0.00	0.00
V_2O_3	0.00	0.00	0.00	0.18	0.19	0.23	0.00	0.17
Fe_2O_3	0.58	0.00	0.00	0.00	0.00	0.00	0.00	0.05
Ce_2O_3	0.13	0.14	0.14	0.00	0.00	0.14	0.00	0.00
FeO	43.89	27.58	26.85	22.77	22.18	22.67	16.38	8.06
MnO	2.81	16.76	15.12	15.88	16.34	16.01	19.64	37.67
MgO	0.12	0.00	0.00	0.00	0.00	0.00	0.00	0.00
CaO	0.00	0.00	0.30	0.15	0.14	0.23	0.00	0.00
ZnO	0.00	0.83	2.51	5.41	7.09	8.21	9.50	1.04
Total	99.69	98.09	97.77	98.93	99.72	99.62	97.38	99.27
			Content of ions on the basis of 3 O pfu					
W^{6+}	0.000	0.000	0.000	0.000	0.000	0.000	0.000	0.003
Nb^{5+}	0.007	0.015	0.027	0.030	0.015	0.007	0.010	0.005
Ta^{5+}	0.002	0.002	0.007	0.005	0.001	0.001	0.001	0.000
Ti^{4+}	0.980	0.991	0.965	0.985	0.998	0.998	0.994	0.985
Al^{3+}	0.000	0.000	0.007	0.000	0.000	0.001	0.006	0.000
Sc^{3+}	0.001	0.000	0.000	0.000	0.000	0.000	0.000	0.000
V^{3+}	0.000	0.000	0.000	0.004	0.004	0.005	0.000	0.003
Fe^{3+}	0.011	0.000	0.000	0.000	0.000	0.000	0.000	0.001
Ce^{3+}	0.001	0.001	0.001	0.000	0.000	0.001	0.000	0.000
Fe^{2+}	0.933	0.593	0.584	0.487	0.470	0.485	0.358	0.171
Mn^{2+}	0.060	0.365	0.333	0.344	0.351	0.347	0.434	0.812
Mg^{2+}	0.005	0.000	0.000	0.000	0.000	0.000	0.000	0.000
Ca^{2+}	0.000	0.000	0.008	0.004	0.004	0.006	0.000	0.000
Zn^{2+}	0.000	0.016	0.048	0.102	0.133	0.155	0.183	0.020
Σ cations	*2.000*	*1.983*	*1.980*	*1.961*	*1.976*	*1.996*	*1.986*	*2.000*
O^{2-}	3	3	3	3	3	3	3	3
Mn/(Mn+Fe)	*0.060*	*0.381*	*0.363*	*0.414*	*0.427*	*0.417*	*0.548*	*0.825*
Ta/(Ta+Nb)	*0.229*	*0.126*	*0.213*	*0.150*	*0.070*	*0.149*	*0.114*	*0.000*

Note: Zr, Sn and REE (except for Ce) are below detection.
Abbreviations: Ilm - ilmenite, Prf - pyrophanite

the core, with blue-olive pleochroism constitutes a transitional subzone with slightly higher Ti, up to 0.040 *apfu* (Ib in Tab. 7 and Fig. 9). The internal olive-brown part of the mantle has Ti from 0.040 to slightly above 0.090 *apfu* at generally decreasing Mn/(Mn + Fe) from 0.030 to about 0.010. In the outermost zones of some brown tourmaline crystals, the Ti content reaches 0.12–0.15 *apfu* with Mn/(Mn + Fe) decreasing as before down to 0.005. The Fe/Ti ratio ranges from 120–60 in the blue core, through 30–20 in olive, olive-brownish and brownish mantle, to 15–10 in the outermost, brown zone of some Mg-enriched crystals. In accordance with the spectroscopic data of Mattson and Rossman (1987) and da Fonseca-Zang et al. (2008), these data suggest that the internal texture of the tourmaline crystals results mainly from the spin-allowed crystal field transitions of Fe^{2+} and the Fe^{2+}–Fe^{3+} charge-transfer transitions responsible for blue color of the core and the Fe^{2+}–Ti^{4+} charge-transfer transitions responsible for the yellowish-brown to brown color of the mantle. Tourmaline, as in CGM and other Nb–Ta oxides, reflects the reversed Mn–Fe fractionation trend in the transition from the stage of early
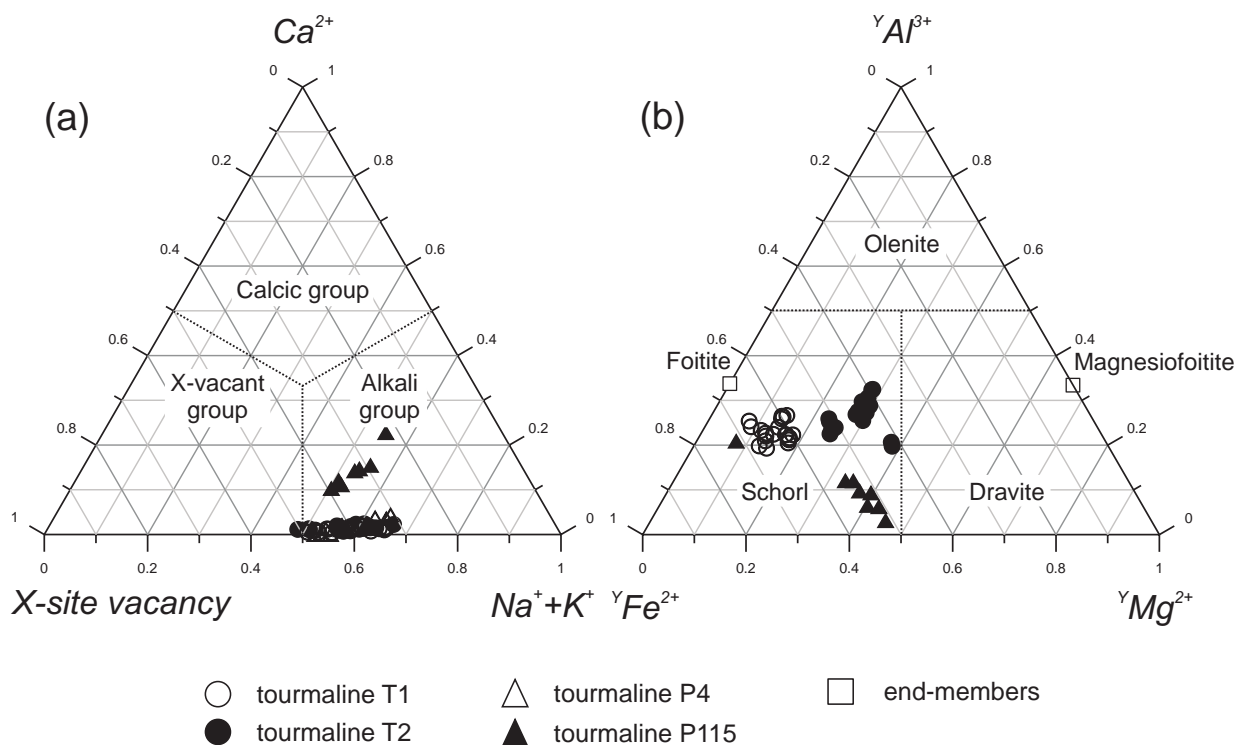
Tab. 6. Representative compositions of biotite

	P2/1A#5	P2/1A#4	P3/2A#1	P3/2A#2	P3/2A#3	T/1A#35	T/1A#37	T/1A#38
	core	rim	core	→	rim	core	→	rim
				wt. %				
SiO_2	36.06	36.04	35.39	35.47	35.14	36.36	36.22	36.35
TiO_2	2.33	1.59	3.85	3.62	3.17	3.66	3.16	2.66
Al_2O_3	17.12	16.95	15.91	15.96	16.34	14.99	15.44	15.94
FeO_{tot}	19.58	20.73	22.90	23.01	23.01	20.70	21.17	20.05
MnO	0.00	0.00	0.34	0.50	0.46	0.00	0.00	0.00
MgO	9.67	9.77	7.89	7.65	7.83	9.62	10.00	10.34
CaO	0.14	0.00	0.00	0.00	0.00	0.00	0.00	0.00
Na_2O	0.00	0.09	0.12	0.10	0.13	0.23	0.14	0.18
K_2O	10.03	9.89	9.44	9.42	9.55	9.31	9.07	9.19
BaO	0.00	0.00	0.12	0.02	0.00	0.00	0.00	0.32
H_2O*	3.90	3.89	3.87	3.86	3.86	3.89	3.90	3.90
Total	98.83	98.95	99.83	99.61	99.48	98.76	99.09	98.93
			Contents of ions on the basis of 22 O apfu					
Si	5.539	5.555	5.480	5.504	5.464	5.611	5.572	5.583
Al^{IV}	2.461	2.445	2.520	2.496	2.536	2.389	2.428	2.417
ΣZ	*8.000*	*8.000*	*8.000*	*8.000*	*8.000*	*8.000*	*8.000*	*8.000*
Al^{VI}	0.638	0.634	0.383	0.423	0.460	0.339	0.372	0.470
Ti	0.269	0.184	0.448	0.423	0.371	0.425	0.365	0.307
Fe^{2+}	2.515	2.672	2.966	2.985	2.992	2.672	2.723	2.576
Mn	0.000	0.000	0.044	0.065	0.061	0.000	0.000	0.000
Mg	2.214	2.245	1.822	1.768	1.816	2.214	2.292	2.367
ΣY	*5.637*	*5.736*	*5.663*	*5.664*	*5.700*	*5.649*	*5.752*	*5.720*
Ca	0.023	0.000	0.000	0.000	0.000	0.000	0.000	0.000
Na	0.000	0.027	0.036	0.031	0.040	0.069	0.042	0.054
K	1.965	1.944	1.864	1.865	1.893	1.832	1.779	1.801
Ba	0.000	0.000	0.007	0.001	0.000	0.000	0.000	0.019
ΣX	*1.988*	*1.971*	*1.908*	*1.897*	*1.934*	*1.902*	*1.821*	*1.874*
Fe/(Fe+Mg)	*0.543*	*0.532*	*0.619*	*0.628*	*0.622*	*0.547*	*0.543*	*0.521*

Note: Rb, Cs, Sn, P and F are below detection limits. All Fe as Fe^{2+}, H_2O based on stoichiometry.

crystallization from Ti-poor melt to the later stage with increasing role of Fe and Ti (and especially Ti relative Fe), and Mn decreasing.

5.3. Garnet

The almandine–spessartine variety of garnet is common in the blocky feldspar zone and the quartz core, where it forms well-developed crystals up to 5 cm across. Oval aggregates of skeletal garnet intergrown with quartz and, more rarely, with microcline and muscovite, up to 10 cm in diameter, were observed in the graphic zone (Szuszkiewicz et al. in print). The primary garnet has negligible Ca and Mg contents and displays a moderate degree of Mn–Fe fractionation with Mn/(Mn + Fe) from ~0.40 to slightly above 0.50 (Tab. 8). It corresponds closely to a degree of Mn–Fe fractionation displayed by crystals of the CGM that occur in the immediate

Tab. 7 Representative compositions of tourmaline

	T1a/11	T1b/20	T2a/4	T2b/10	T2a/3	T1a/12	T1a/3	T2a/7	T2a/8	T2b/12	T2b/9	T1a/2	T1a/4
	Ia	Ia	Ia	Ia	Ib	IIa	IIa	IIa	IIa	IIa	IIa	IIb	IIb
						wt. %							
SiO_2	36.44	36.38	35.68	35.52	35.58	36.04	35.85	35.50	35.24	34.83	35.00	35.50	36.19
TiO_2	0.16	0.14	0.12	0.12	0.24	0.47	0.55	0.49	0.66	0.53	0.64	0.79	0.96
B_2O_3	10.61	10.61	10.39	10.38	10.35	10.57	10.57	10.33	10.32	10.28	10.27	10.45	10.57
Al_2O_3	36.23	35.83	34.49	34.61	34.27	35.65	35.35	33.73	33.77	34.06	34.13	34.61	34.25
FeO	8.48	9.25	12.55	12.29	12.57	8.82	9.47	13.36	13.36	13.32	13.50	10.54	8.69
MnO	0.15	0.09	0.29	0.41	0.25	0.19	0.12	0.30	0.19	0.38	0.38	0.11	0.03
MgO	3.43	3.36	1.66	1.71	1.63	3.51	3.55	1.44	1.48	1.29	0.90	2.95	4.33
CaO	0.06	0.07	0.03	0.03	0.07	0.09	0.14	0.07	0.09	0.11	0.05	0.04	0.12
Na_2O	1.60	1.52	1.52	1.61	1.64	1.83	1.88	1.85	1.89	1.82	1.77	1.78	1.88
K_2O	0.00	0.00	0.07	0.02	0.03	0.04	0.03	0.01	0.03	0.02	0.04	0.00	0.05
H_2O	3.21	3.31	3.32	3.32	3.25	3.18	3.26	3.23	3.21	3.25	3.18	3.26	3.25
Total	100.37	100.59	100.11	100.01	99.88	100.39	100.77	100.28	100.24	99.90	99.84	100.03	100.42
				Content of ions on the basis of 31 (O,OH) and 15 (Y,Z,T) apfu									
Na^+	0.508	0.484	0.492	0.523	0.534	0.583	0.601	0.602	0.619	0.596	0.579	0.575	0.600
K^+	0.000	0.000	0.015	0.005	0.007	0.008	0.006	0.001	0.007	0.004	0.009	0.000	0.010
Ca^{2+}	0.011	0.011	0.005	0.005	0.012	0.016	0.024	0.012	0.016	0.020	0.008	0.007	0.022
vacancy	0.481	0.505	0.488	0.467	0.447	0.393	0.369	0.385	0.358	0.380	0.404	0.418	0.368
ΣX	*1.000*	*1.000*	*1.000*	*1.000*	*1.000*	*1.000*	*1.000*	*1.000*	*1.000*	*1.000*	*1.000*	*1.000*	*1.000*
$^YAl^{3+}$	0.901	0.882	0.774	0.779	0.759	0.841	0.743	0.657	0.636	0.670	0.727	0.691	0.524
$^YMn^{2+}$	0.021	0.013	0.041	0.058	0.035	0.026	0.017	0.042	0.028	0.055	0.054	0.015	0.005
$^YFe^{2+}$	1.161	1.267	1.757	1.721	1.765	1.214	1.302	1.879	1.881	1.882	1.911	1.466	1.196
$^YMg^{2+}$	0.837	0.820	0.413	0.427	0.409	0.861	0.870	0.361	0.371	0.325	0.227	0.730	1.087
$^YTi^{4+}$	0.020	0.018	0.015	0.015	0.031	0.058	0.068	0.061	0.084	0.068	0.081	0.098	0.118
ΣY	*3.000*	*3.000*	*3.000*	*3.000*	*3.000*	*3.000*	*3.000*	*3.000*	*3.000*	*3.000*	*3.000*	*3.000*	*3.000*
$^ZAl^{3+}$	6.000	6.000	6.000	6.000	6.000	6.000	6.000	6.000	6.000	6.000	6.000	6.000	6.000
B^{3+}	3.000	3.000	3.000	3.000	3.000	3.000	3.000	3.000	3.000	3.000	3.000	3.000	3.000
$^TSi^{4+}$	5.968	5.960	5.971	5.948	5.976	5.928	5.894	5.971	5.934	5.887	5.922	5.905	5.954
$^TAl^{3+}$	0.032	0.040	0.029	0.052	0.024	0.072	0.106	0.029	0.066	0.113	0.078	0.095	0.046
ΣT	*6.000*	*6.000*	*6.000*	*6.000*	*6.000*	*6.000*	*6.000*	*6.000*	*6.000*	*6.000*	*6.000*	*6.000*	*6.000*
O^{2-}	27.497	27.384	27.292	27.296	27.363	27.509	27.428	27.378	27.396	27.331	27.416	27.382	27.438
OH^-	3.503	3.616	3.708	3.704	3.637	3.491	3.572	3.622	3.604	3.669	3.584	3.618	3.562
Mn/(Mn+Fe)	*0.018*	*0.010*	*0.015*	*0.015*	*0.031*	*0.021*	*0.013*	*0.022*	*0.014*	*0.028*	*0.027*	*0.010*	*0.004*

neighborhood of, or form inclusions in, the garnet. Some crystals show an 'island' texture with numerous relics of the primary almandine–spessartine garnet cross-cut by a younger Ca-enriched spessartine (Fig. 13). The younger generation of garnet displays somewhat higher Mn/(Mn + Fe) values of 0.60–0.63. The internal texture of such crystals and the distinct decrease in Fe^{2+} in the secondary garnet suggest metasomatic replacement of Fe^{2+} by Ca^{2+} along a net of random fractures in the primary garnet crystals.

6. Concluding remarks

The Fe^{2+}–Mn^{2+} balance in the melt changed due to the appearance of additional Fe, Ti, Mg and Ca and the preferred incorporation of Fe^{2+} over Mn^{2+} by the CGM. Increasing abundances of Ti^{4+}, Sn^{4+}, Fe^{3+} and Sc^{3+} during late stages of columbite-(Fe) – columbite-(Mn) crystallization resulted also from the *euxenite*-type substitution $R^{2+} + R^{5+} \leftrightarrow R^{3+} + R^{4+}$. This mechanism led finally to the crystallization of ixiolite and ferrowodginite. A progressive increase in Ti^{4+} content of the melt is marked by the composition of tourmaline associated with the CGM, whereas the increasing activity of Mg and/or Ca is reflected by Ca-enriched schorl evolving to dravite, metasomatic alteration of primary almandine–spessartine garnet to Ca-bearing spessartine, alterations of primary CGM and by crystallization of secondary Ca-rich members of the pyrochlore, microlite and betafite groups at the expense of columbite-, samarskite- and euxenite-group minerals.

The anomalies in Mn–Fe and Ta–Nb fractionation in Nb–Ta minerals can be explained by (1) *in situ* contamination of the pegmatite-forming melt by the sur-

⇦

Fig. 10 Ternary plots of tourmaline compositions from the Julianna-type dykes: **a** – X-site vacancy–Ca^{2+}–(Na + K)$^+$; **b** – ^YFe –^YAl–^YMg.
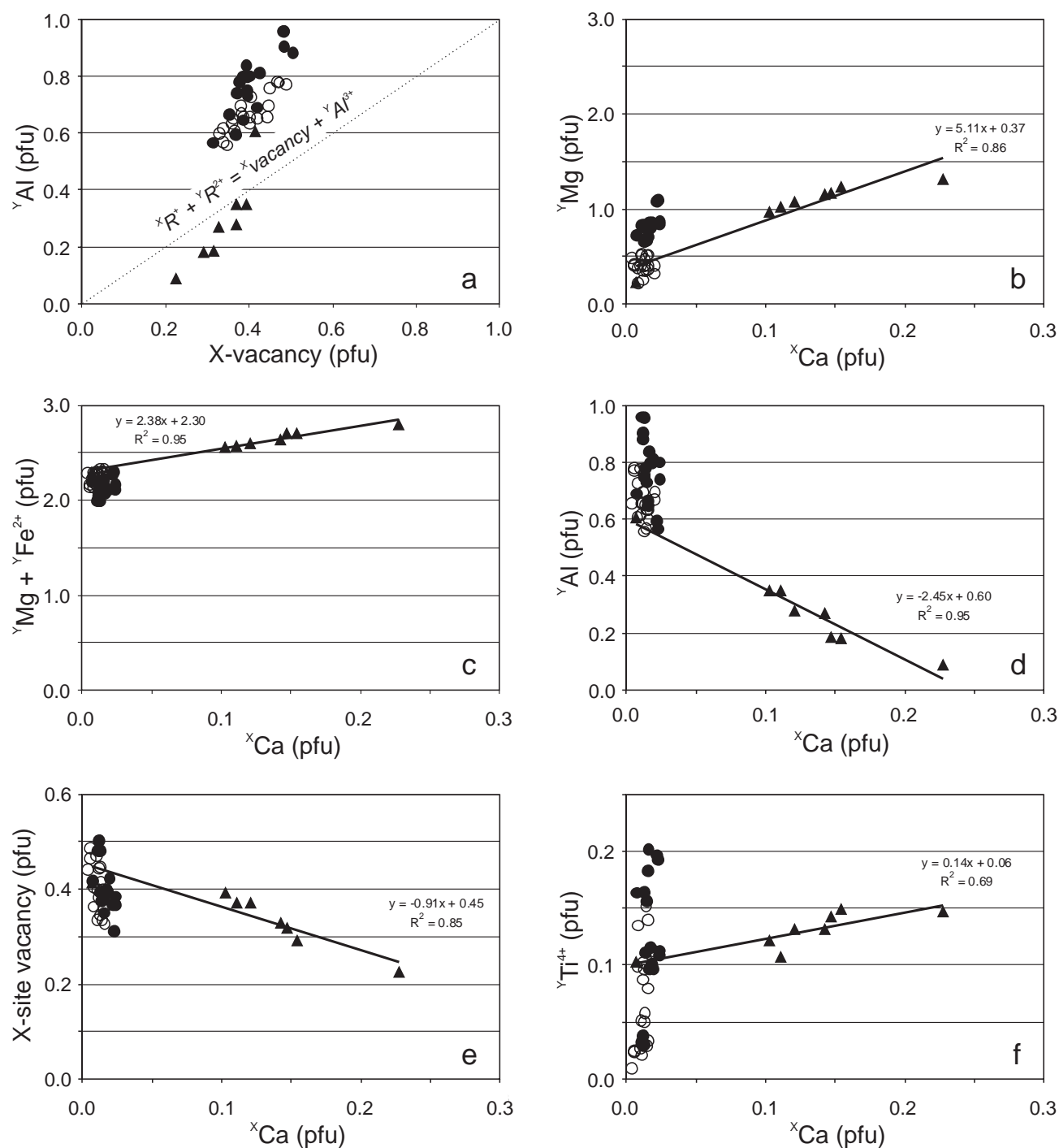
Fig. 11 Compositional relationships in tourmalines from the Julianna-type dykes and veins: **a** – ^{Y}Al vs. X-site vacancy; **b** – ^{Y}Mg vs. ^{X}Ca; **c** – ^{Y}(Mg + Fe^{2+}) vs. ^{X}Ca; **d** – ^{Y}Al vs. ^{X}Ca; **e** – X-site vacancy vs. ^{X}Ca; **f** – ^{Y}Ti^{4+} vs. ^{X}Ca. Symbols as in Fig. 10.
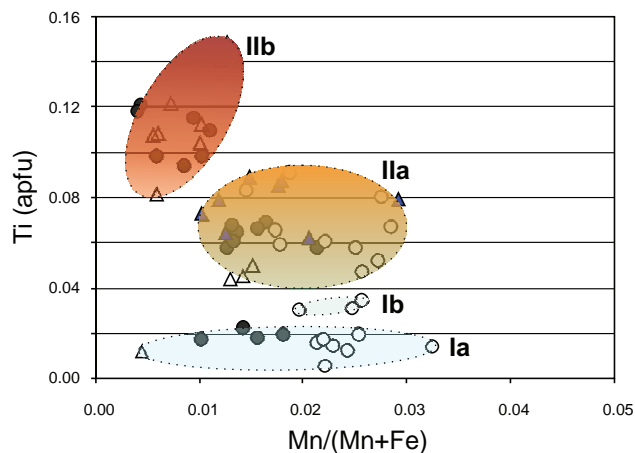
rounding host rocks (e.g. Galliski et al. 2008; Novák et al. 2012), (2) pre-emplacement contamination of the pegmatite-forming melt, (3) influx of a more primitive pegmatitic melt, (4) competition for the elements among co-crystallizing minerals, and (5) local changes in melt composition.

Contamination of the parental pegmatite-forming melt by host rocks could have easily supplied additional Fe, Mg, Ti, Sn, Ca and some other elements released by the breakdown of biotite, plagioclase, accessory ilmenite and other oxides present in the surrounding amphibolites. However, real evidence for a significant interaction between the peg-

Tab. 8 Representative compositions of garnet

	P110	P111	P113a	P113b	P127a	P127b
			wt. %			
SiO_2	36.33	35.83	35.89	36.83	36.15	36.59
TiO_2	0.02	0.08	0.06	0.12	0.00	0.00
Al_2O_3	20.94	20.57	20.44	20.90	20.83	20.76
Fe_2O_3	0.00	0.90	0.94	0.98	0.26	1.42
FeO	24.53	16.86	20.89	14.66	20.75	11.26
MnO	18.61	26.16	21.98	18.26	22.18	21.00
CaO	0.21	0.18	0.19	8.72	0.20	9.24
MgO	0.06	0.03	0.10	0.20	0.11	0.11
Total	100.70	100.61	100.49	100.68	100.48	100.39
		Content of ions on the basis of 12 O apfu				
Fe^{2+}	1.683	1.161	1.441	0.986	1.427	0.760
Mn^{2+}	1.293	1.825	1.536	1.243	1.545	1.435
Ca^{2+}	0.018	0.016	0.017	0.751	0.018	0.798
Mg^{2+}	0.008	0.004	0.012	0.024	0.014	0.014
ΣA site	*3.003*	*3.006*	*3.005*	*3.004*	*3.004*	*3.007*
Al^{3+}	2.001	1.944	1.941	1.937	1.987	1.919
Fe^{3+}	0.000	0.056	0.058	0.060	0.016	0.086
Ti^{4+}	0.001	0.005	0.004	0.007	0.000	0.000
ΣB site	*2.002*	*2.004*	*2.003*	*2.003*	*2.002*	*2.004*
Si^{4+}	2.980	2.952	2.960	2.961	2.972	2.952
Al^{3+}	0.023	0.054	0.045	0.043	0.032	0.055
ΣT site	*3.003*	*3.006*	*3.005*	*3.004*	*3.004*	*3.007*
O^{2-}	12	12	12	12	12	12
Mn/(Mn+Fe)	*0.435*	*0.600*	*0.506*	*0.543*	*0.517*	*0.629*

Fig. 12 A correlation between (ω) pleochroic color of the Julianna-type tourmaline and its composition expressed in binary plot of Ti (*in apfu*) vs. Mn/(Mn + Fe), the latter expressing the Mn–Fe fractionation. Symbols as in Fig. 10, Ia and Ib – the crystal core, IIa and IIb – the rim.

matite and its wall rocks is rather weak. Nevertheless, contamination of the parental pegmatite-forming melt could have taken place in a hypothetical reservoir of the anatectic melt or along the melt's migration path before emplacement. This hypothesis needs further investigation, as no evidence of a late influx of more primitive pegmatitic melt into the Julianna system has been found so far. Readjustment of the compositions of early crystallized biotite and Ca-rich plagioclase (andesine to oligoclase) of the outer pegmatitic zones to the changing physical and chemical conditions of the rapidly cooling melt could supply elements such as Ca (from plagioclase), Ti and possibly also Mg and Fe (from biotite) to minerals forming in the inner zones of the pegmatites. Such intra-pegmatite element recycling would be more efficient in the largest veins with well-developed textural differentiation and would depend strongly on the lifetime of the pegmatite body. The process was certainly intensified at the hydrothermal stage by alteration, such as the commonly observed chloritization of biotite, albitization and sericitization of plagioclase. Local changes in melt composition had rather second-rank importance, e.g. locally high Ca activity could have induced the crystallization of Ca-rich tourmaline associated with other Ca-rich phases like titanite or epidote-group minerals. A limitation in Ta accessibility seems to have been the main factor in the only incidentally noted progressive Ta–Nb fractionation in columbite-(Fe) from the transition between the graphic and massive feldspar intermediate zones. On the other hand, Nb–Ta oxides that display the most continuous trend IIb from the progressive through the reversed Mn–Fe fractionation (CGM evolving to ixiolite, and ferrowodginite), are those which could evolve in residual melt particularly enriched in volatiles (B_2O_3, H_2O). Their occurrence is commonly connected with small nest-like aggregates composed mainly of tourmaline, garnet, abundant muscovite and quartz, where H_2O activity in the melt was the highest during the pegmatite consolidation and the melt could exist for the longest time.
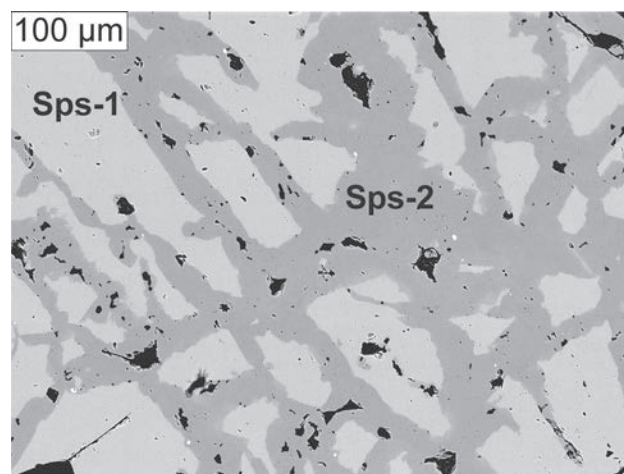
Fig. 13 A back-scattered electron (BSE) image of the 'island' texture in garnet. Abbreviations: Sps-1 – Ca–Mg-poor spessartine, Sps-2 – Ca-rich spessartine.

References

Aftalion M, Bowes DR (2002) U–Pb zircon isotopic evidence for Mid-Devonian migmatite formation in the Góry Sowie domain of the Bohemian Massif, Sudeten Mountains, SW Poland. Neu Jb Mineral, Mh 4: 182–192

Baldwin JR (1989) Replacement phenomena in tantalum minerals from rare-metal pegmatites in South Africa and Namibia. Mineral Mag 53: 571–581

Beurlen H, Barreto SB, Silva D, Wirth R, Olivier P (2007) Titanian ixiolite–niobian rutile intergrowths from the Borborema Pegmatitic Province, northeastern Brazil. Canad Mineral 45: 1367–1387

Beurlen H, Da Silva MRR, Thomas R, Soares DR, Oliver P (2008) Nb–Ta–(Ti–Sn) oxide mineral chemistry as tracer of rare-element granitic pegmatite fractionation in the Borborema Province, northeastern Brazil. Miner Depos 43: 207–228

Bröcker M, Żelaźniewicz A, Enders M (1998) Rb–Sr and U–Pb geochronology of migmatitic gneisses from the Góry Sowie (West Sudetes, Poland): the importance of Mid–Late Devonian metamorphism. J Geol 155: 1025–1036

Brueckner HK, Blusztajn J, Bakun-Czubarow N (1996) Trace element and Sm–Nd "age" zoning in garnets from peridotites of the Caledonian and Variscan mountains and tectonic implications. J Metamorph Geol 14: 61–73

Černý P, Ercit TS (2005) The classification of granitic pegmatites revisited. Canad Mineral 43: 2005–2026

Černý P, Novák M, Chapman R (1992) Effects of sillimanite-grade metamorphism and shearing on Nb–Ta oxide minerals in granitic pegmatites, Maršíkov, northern Moravia, Czechoslovakia. Canad Mineral 30: 699–718

Černý P, Chapman R, Ferreira K, Smeds SA (2004) Geochemistry of oxide minerals of Nb, Ta, Sn, and Sb in the Varuträsk granitic pegmatite, Sweden: the case of "anomalous" columbite–tantalite trend. Amer Miner 89: 505–518

da Fonseca-Zang WA, Zang JW, Hofmeister W (2008) The Ti-influence on the tourmaline colour. J Brazil Chem Soc 19: 1186–1192

Dathe E, Finckh L (1924) Erläuterungen zu Blatt Charlottenbrunn. Geologische Karte von Preußen und benachbarten deutschen Ländern 1:25 000. Lief 254. Preussisches Geologisches Landesamt, Berlin

Ercit TS, Černý P, Hawthorne FC, McGammon CA (1992) The wodginite group. II. Crystal chemistry. Canad Mineral 30: 613–631

Fiedler H (1863) Die Mineralien Schlesiens mit Berücksichtigung der angrenzenden Länder. F. E. C. Leuckart, Breslau, pp 1–100

Galliski MA, Marquez-Zavalía MF, Černý P, Martinez VA, Chapman R (2008) The Ta–Nb–Sn–Ti oxide-mineral paragenesis from LaViquita, a spodumene-bearing rare-element granitic pegmatite, San Luis, Argentina. Canad Mineral 46: 379–393

Gordon SM, Schneider DA, Manecki M, Holm DK (2005) Exhumation and metamorphism of an ultrahigh-grade terrane: geochronometric investigations of the Sudetes Mountains (Bohemia), Poland and Czech Republic. J Geol Soc, London 162: 841–855

Grocholski W (1967) Structure of the Sowie Mts. Geol Sudetica 3: 181–249 (in Polish, English summary)

Gunia T (1985) Geological position of the Sowie Góry Block and its influence on the paleogeography of the Paleozoic of Central Sudetes. Geol Sudetica 20: 83–119 (in Polish, English summary)

Gunia P (1997) Petrology of ultrabasic rocks from the Góry Sowie Block. Prace Geol Miner 65: 1–78 (in Polish, English summary)

Hintze C (1933) Handbuch der Mineralogie, Bd. 1/4, Cruyter and Co., Berlin und Leipzig

Ilnicki S, Nejbert K, Pieczka A, Szełęg E, Turniak K, Szuszkiewicz A, Łodziński M, Banach M, Michałowski P, Różniak R (2010) Eclogites from the Piława Górna quarry (Dolnośląskie Surowce Skalne S.A.), Góry Sowie Block, SW Poland: a preliminary report. Miner Spec Papers 37: 81

Keppler H (1993) Influence of fluorine on the enrichment of high field strength trace elements in granitic rocks. Contrib Mineral Petrol 114: 479–488

Kröner A, Hegner E (1998) Geochemistry, single zircon ages and Sm–Nd systematics of granitoid rocks from the Góry Sowie (Owl Mts.), Polish West Sudetes: evidence for early Palaeozoic arc-related plutonism. J Geol Soc, London 155: 711–724

Kryza R (1981) Migmatization in gneisses of the northern part of the Sowie Góry, Sudetes. Geol Sudetica 16: 7–91 (in Polish, English summary)

Kryza R, Fanning CM (2007) Devonian deep-crustal metamorphism and exhumation in the Variscan Orogen: evidence from SHRIMP zircon ages from the HT–HP granulites and migmatites of the Góry Sowie (Polish Sudetes). Geodin Acta 20: 159–176

Linnen RL (1998) The solubility of Nb–Ta–Zr–Hf–W in granitic melts with Li and Li + F: constraints for mineralization in rare metal granites and pegmatites. Econ Geol 93: 1013–1025

Linnen RL, Keppler H (1997) Columbite solubility in granitic melts: consequences for the enrichment and

fractionation of Nb and Ta in the Earth's crust. Contrib Mineral Petrol 128: 213–227

Łodziński M, Pieczka A (2008) (Nb–Ta)-oxide minerals from pegmatites of the Owiesno–Kietlice area in the Sowie Mts block, Southwestern Poland. Miner Spec Papers 32: 108

Łodziński M, Pieczka A, Szełęg E, Nejbert K, Szuszkiewicz A, Turniak K, Ilnicki S, Banach M, Michałowski P, Różniak R (2010) Beryllium minerals (beryl, phenakite and bavenite) in pegmatites of the DSS mine at Piława Górna, Góry Sowie block, SW Poland. Miner Spec Papers 37: 91–92

Mattson SM, Rossman GR (1987) Identifying characteristics of charge transfer transitions in minerals. Phys Chem Miner 14: 94–99

Morawski T (1973) The Sowie Góry area and its petrological problems. In: Smulikowski K (ed) Revue des problèms géologiques des zones profondes de l'écorce terrestre en Basse Silesie. Wydawnictwa Geologiczne, Warszawa, pp 44–58

Nejbert K, Pieczka A, Szełęg E, Ilnicki S, Szuszkiewicz A, Łodziński M, Turniak K, Banach M, Michałowski P, Różniak R (2010) Textural and chemical varieties of garnets in the pegmatites from Piława Górna quarry (Dolnośląskie Surowce Skalne S.A.), Góry Sowie Block, southwestern Poland. Miner Spec Papers 37: 96

Novák M (2005) Granitic pegmatites of the Bohemian Massif (Czech Republic); mineralogical, geochemical and regional classification and geological significance Acta Mus Moraviae, Sci Geol 90: 3–75 (in Czech with English summary)

Novák M, Čech F (1995) Scandian columbite and niobian rutile from pegmatites penetrating the Třebíč durbachite massif, western Moravia, Czech Republic. Acta Mus Moraviae, Sci Nat 80: 3–8

Novák M, Černý P (2001) Distinctive compositional trends in columbite–tantalite from two segments of the lepidolite pegmatite at Rožná, western Moravia, Czech Republic. J Czech Geol Soc 46: 1–8

Novák M, Černý P, Uher P (2003) Extreme variation and apparent reversal of Nb–Ta fractionation in columbite-group minerals from the Scheibengraben beryl–columbite pegmatite, Maršíkov, Czech Republic. Eur J Mineral 15: 565–574

Novák M, Škoda R, Gadas P, Krmíček L, Černý P (2012) Contrasting origin of the mixed (NYF + LCT) signature in granitic pegmatites, with examples from the Moldanubian Zone, Czech Republic. Canad Mineral 50: 1077–1094

O'Brien PJ, Kröner A, Jaeckel P, Hegner E, Żelaźniewicz A, Kryza R (1997) Petrological and isotope studies on Palaeozoic high-pressure granulites. Góry Sowie Mts, Polish Sudetes. J Petrol 38: 433–456

Pieczka A (2010) Primary Nb–Ta minerals in the Szklary pegmatite, Poland: new insights into controls of crystal chemistry and crystallization sequences. Amer Miner 95: 1478–1492

Pieczka A, Gołębiowska B, Skowroński A (2003) Ferris-icklerite and other phosphate minerals from the Lutomia pegmatite (SW Poland, Lower Silesia, Góry Sowie Mts). In: Cempírek J (ed) International Symposium on Light Elements in Rock-Forming Minerals, Nové Město na Moravě, Czech Republic, June 20 to 25, 2003, Book of Abstracts. Masaryk University & Moravian Museum, Brno, pp 63–64

Pieczka A, Łobos K, Sachanbiński M (2004) The first occurrence of elbaite in Poland. Miner Pol 35: 3–14

Pieczka A, Szełęg E, Szuszkiewicz A, Łodziński M, Nejbert K, Turniak K, Ilnicki S, Banach M, Michałowski P, Różniak R (2010) Lithium pegmatite from the DSS Piława Górna mine, Góry Sowie Block, southwestern Poland. Mineral Spec Papers 37: 99

Pieczka A, Łodziński M, Szełęg E, Ilnicki S, Nejbert K, Szuszkiewicz A, Turniak K, Banach M, Michałowski P, Różniak R (2012) The Sowie Mts. pegmatites (Lower Silesia, SW Poland): a current knowledge. Acta Mineral Petrograph, Abstract Series 7: 105–106

Polański A. (1955) On the metamorphism of crystalline formations of the Sowie Mts (Middle Sudeten). Arch Mineral 18: 211–284 (in Polish, English summary)

Pouchou IL, Pichoir F (1985) "PAP" (ϕ–ρ–Z)) procedure for improved quantitative microanalysis. In: Armstrong IT (ed) Microbeam Analysis. San Francisco Press, San Francisco, pp 104–106

Römer F (1864) Über die Auffindung des Columbit. Jahres-berichte der schlesischen Gesellschaft für vaterländische Cultur 41: 35

Roth J (1867) Erläuterungen zu der geognostischen Karte von Niederschlesichen Gebirge und den umliegenden Gegenden Berlin, Neumann [8] ss. XX, 396

Szełęg E, Szuszkiewicz A, Pieczka A, Nejbert K, Turniak K, Łodziński M, Ilnicki S (2010) Geology of the Julianna pegmatite vein system from the Piława Górna quarry (Dolnośląskie Surowce Skalne S.A.), Sowie Mountains Block, SW Poland. Mineral Spec Papers 37: 111

Szuszkiewicz A, Szełęg E, Pieczka A, Ilnicki S, Nejbert K, Turniak K, Banach M, Łodziński M, Różniak R, Michałowski P (in print) The Julianna pegmatite vein system at the Piława Górna mine, Góry Sowie Block, SW Poland – preliminary data on geology and descriptive mineralogy. Geol Q 57: doi: 10.7306/gq.1097

Timmermann H, Parrish RR, Noble SR, Kryza R (2000) New U–Pb monazite and zircon data from the Sudetes Mountains in SW Poland; evidence for a single-cycle Variscan Orogeny. J Geol Soc, London 157: 265–268

Tindle AG, Breaks FW (1998) Oxide minerals of the Separation Rapids rare-element granitic pegmatite

group, northwestern Ontario. Canad Mineral 36: 609–635

Tindle AG, Breaks FW (2000) Columbite–tantalite mineral chemistry from rare-element granitic pegmatites: Separation Lake area, N.W. Ontario, Canada. Mineral Petrol 70: 165–198.

Traube H (1888) Die Minerale Schlesiens. M. Müller, Breslau, pp 1–286

Van Breemen O, Bowes DR, Aftalion M, Żelaźniewicz A (1988) Devonian tectonothermal activity in the Sowie Góry gneissic block, Sudetes, southwestern Poland: evidence from Rb–Sr and U–Pb isotopic studies. J Pol Geol Soc 58: 3–10

Van Lichtervelde M, Salvi S, Beziat D (2007) Textural features and chemical evolution in tantalum oxides: magmatic versus hydrothermal origin for Ta mineralization in the Tanco Lower pegmatite, Manitoba, Canada. Econ Geol 102: 257–276

Websky M (1868) Über Sarkopsid und Kochelite, zwei neue Minerale aus Schlesien. Z Dtsch Geol Gesell 20: 245–257

Wise MA, Černý P, Falster AU (1998) Scandium substitution in columbite-group minerals and ixiolite. Canad Mineral 36: 673–680

Żelaźniewicz A (1987) Tectonic and metamorphic evolution of the Góry Sowie, Sudetes Mts, SW Poland. J Pol Geol Soc 57: 203–348

Żelaźniewicz A (1990) Deformation and metamorphism in the Góry Sowie gneiss complex, Sudetes, SW Poland. Neu Jb Geol Paläont, Abh 179: 129–157

Żelaźniewicz A (1997) The Sudetes as a Paleozoic orogen in central Europe. Geol Mag 134: 691–702